Monthly Notices of the ROYAL ASTRONOMICAL SOCIETY

MNRAS **508,** 3710–3729 (2021) https://doi.org/10.1093/mnras/stab2772
Advance Access publication 2021 October 2

# The influence of the environment on the spin evolution of low-mass stars – I. External photoevaporation of circumstellar discs

J. Roquette [1]★ S. P. Matt,[1] A. J. Winter [2] L. Amard [1] and S. Stasevic[1]

[1]*Department of Physics & Astronomy, University of Exeter, Stocker Road, EX44QL Exeter, UK*
[2]*Institut für Theoretische Astrophysik, Zentrum für Astronomie, Heidelberg University, Albert Ueberle Str. 2, D-69120 Heidelberg, Germany*

Accepted 2021 September 22. Received 2021 September 22; in original form 2021 August 12

## ABSTRACT

Massive stars are strong sources of far-ultraviolet radiation that can be hostile to the evolution of protoplanetary discs, driving mass-loss by external photoevaporation and shortening disc-dissipation time-scales. Their effect may also reduce the time-scale of angular momentum exchanges between the disc and host star during the early pre-main-sequence phase. To improve our understanding of the environmental influence on the rotational history of stars, we developed a model that considers the influence of the local far-ultraviolet radiation on the spin evolution of low mass stars. Our model includes an assumption of disc locking, which fixes the rotation rate during the star-disc-interaction phase, with the duration of this phase parametrized as a function of the local far-ultraviolet radiation and stellar mass (in the range of 0.1–1.3 $M_{\odot}$). In this way, we demonstrate how the feedback from massive stars can significantly influence the spin evolution of stars and explain the mass dependence observed in period-mass distributions of young regions like Upper Sco and NGC 2264. The high far-ultraviolet environments of high-mass stars can skew the period distribution of surrounding stars towards fast-rotation, explaining the excess of fast-rotating stars in the open cluster h Per. The proposed link between rotation and the pre-main-sequence environment opens new avenues for interpreting the rotational distributions of young stars. For example, we suggest that stellar rotation may be used as a tracer for the primordial ultraviolet irradiation for stars up to ∼1 Gyr, which offers a potential method to connect mature planetary systems to their birth environment.

**Key words:** stars: evolution – stars: low-mass – stars: pre-main-sequence – stars: rotation – stars: solar-type.

## 1 INTRODUCTION

Over the last couple of decades, a growing number of studies have been exploring the influence of the environment on the evolution and dissipation of protoplanetary discs (e.g. Bally et al. 1998; Johnstone, Hollenbach & Bally 1998; Adams et al. 2004; Adams 2010; Facchini, Clarke & Bisbas 2016; Nicholson et al. 2019; Haworth & Clarke 2019; Sellek, Booth & Clarke 2020; Parker, Nicholson & Alcock 2021). Of particular importance is the existence of massive stars in a cluster's population (Adams et al. 2004; Winter et al. 2018). These massive stars can radically influence their surrounding environment due to their strong far-ultraviolet (FUV) emission. FUV photons ($6eV < h\nu < 13.6eV$) can dissociate $H_2$ molecules and trigger the external photoevaporation of the material in protoplanetary discs around neighbouring low mass stars, shortening the time-scales of disc evolution and dissipation (Adams et al. 2004; Winter et al. 2020a; Concha-Ramírez et al. 2021). A number of studies have observationally explored the indirect consequences of external photoevaporation of discs, such as the study of proplyd objects in the neighbourhood of massive stars (Smith, Bally & Morse 2003; Balog et al. 2006; Rigliaco et al. 2009; Wright et al. 2012; Mann et al. 2014; Guarcello et al. 2014; Kim et al. 2016; Haworth et al. 2021) and variations of the disc-fraction and disc-masses of stars in clusters, depending on their proximity to massive stars (Balog et al. 2007; Guarcello et al. 2010; Fang et al. 2012; Guarcello et al. 2016; Ansdell et al. 2017; Eisner et al. 2018). Because of its importance on constraining the time-scales for planet-formation (e.g. Armitage 2000; Najita & Kenyon 2014; Concha-Ramírez et al. 2019b; Ansdell et al. 2020), the dependence of the disc-dissipation time-scales with the local FUV flux has been recently theoretically investigated by a number of authors (e.g. Adams et al. 2004; Facchini et al. 2016; Haworth et al. 2018b; Winter et al. 2018; Concha-Ramírez, Vaher & Portegies Zwart 2019a; Winter et al. 2020a; Sellek et al. 2020; Parker et al. 2021).

External photoevaporation of discs will also shorten the star-disc-interaction (SDI) phase. During this phase, the magnetic interaction between stars and their accretion discs leads to an exchange of mass and angular momentum between the two (e.g. Ghosh & Lamb 1979; Koenigl 1991; Ireland et al. 2021). Stars lose the vast majority of their angular momentum during their first ∼10 Myr, and it is thought that the SDI is the primary driver of the stars' angular momentum evolution (Bodenheimer 1995; Mathieu 2004; Bouvier et al. 2014). Physical models for the magnetic SDI show that the net result of this interaction can either spin-up or spin-down the star, driving the star's rotation toward an equilibrium spin rate (Ghosh & Lamb 1979; Matt & Pudritz 2005; Zanni & Ferreira 2009, 2013; Ireland et al. 2021). In this theoretical equilibrium state, the rotation rate of the star is dictated by a balance of torques, which is determined by physical parameters such as the accretion rate and stellar magnetic field strength. The existence of an equilibrium spin rate is often simplified by an assumption, called 'disc locking' (Edwards et al. 1993), that the rotation rate of a star will remain constant for the duration of the accreting phase, i.e., for the lifetime of the disc (Bouvier, Forestini & Allain 1997; Tinker, Pinsonneault & Terndrup

★ E-mail: jt574@exeter.ac.uk

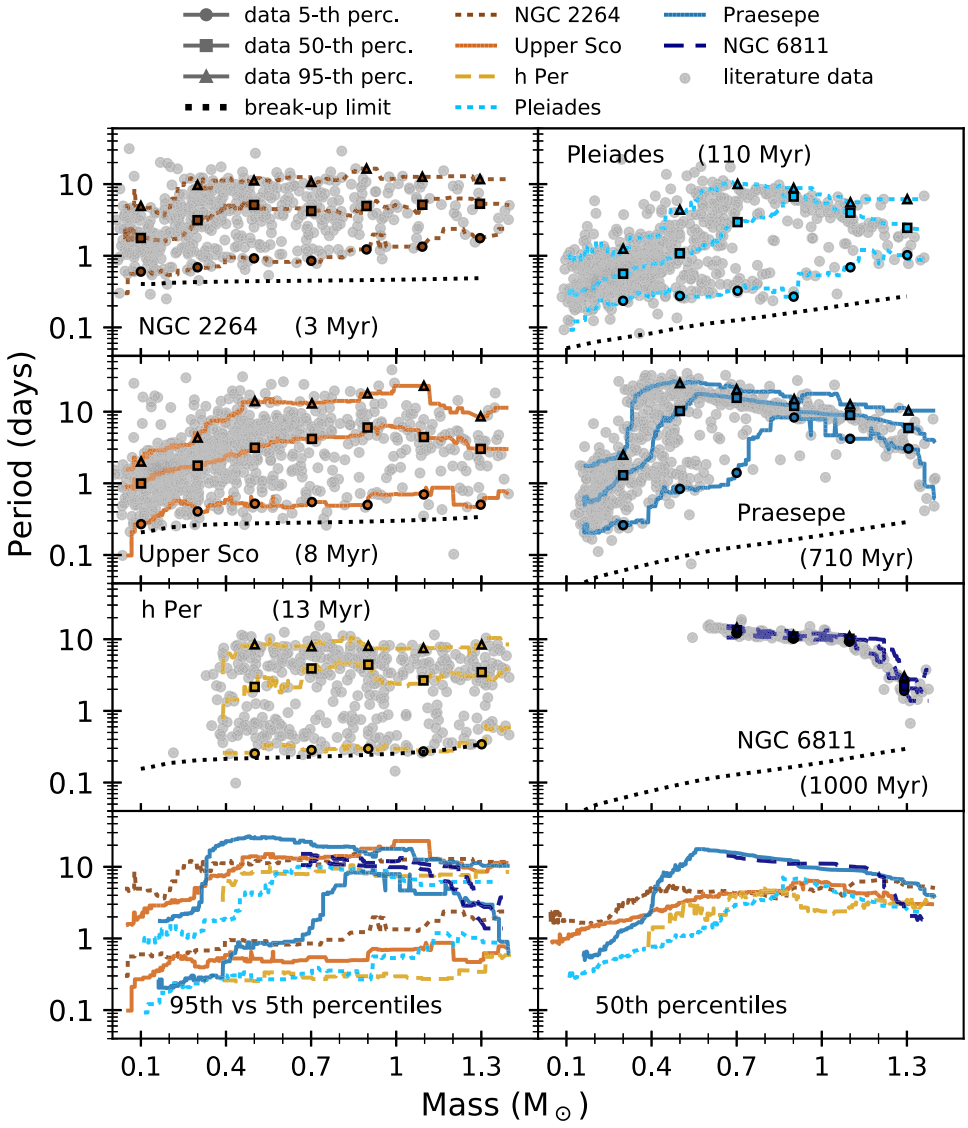


**Figure 1.** Observed rotational period distributions of low mass stars ($M_* \leq 1.4 M_\odot$) in clusters and associations at 3 Myr (NGC 2264), 8 Myr (Upper Sco), 13 Myr (h Per), 110 Myr (Pleiades), 710 Myr (Praesepe), and 1000 Myr (NGC 6811). Observed rotational periods are plotted as a function of stellar mass. Panels are ordered as a function of age. The dashed lines show the break-up limit at each age. The dashed-symbol lines show the 5th (circle), 50th (square), and 95th (triangle) rolling percentiles of the period-mass distributions. The bottom panels show a comparison between the rolling percentiles of clusters at different ages. The outlines of the distributions (5th and 95th rolling percentiles) are compared in the bottom left-hand panel, and their moving averages (50th rolling percentile) are compared in the bottom right-hand panel. Masses are derived as described in Appendix A.

2002; Rebull, Wolff & Strom 2004). Therefore, by impacting the disc lifetime and duration of the SDI, the influence of the environment on the disc-dissipation time-scales should also impact the host stars' angular momentum evolution.

The importance of the SDI for removing angular momentum is supported by a growing number of observational studies in star-forming regions, which typically find a positive correlation between slow-rotation and the presence of a disc for solar-type stars ($M_*$ $\sim$ 0.3−1.3 $M_\odot$) along with statistically relevant differences in the distributions of observed spin rates for coeval stars with and without discs (e.g. Attridge & Herbst 1992; Edwards et al. 1993; Rebull et al. 2004, 2006; Cieza & Baliber 2007; Irwin et al. 2008; Rodríguez-Ledesma, Mundt & Eislöffel 2010; Roquette et al. 2017; Venuti et al. 2017; Rebull et al. 2018, 2020). The observational scenario is less settled for very low-mass stars ($M_* < 0.3$ $M_\odot$), and although most observational studies in this mass regime also point to a correlation between rotation and the presence of a disc (Scholz & Eislöffel 2004; Scholz et al. 2015; Venuti et al. 2017; Moore, Scholz & Jayawardhana 2019; Rebull et al. 2018, 2020), this correlation is not observed in all circumstances (Lamm et al. 2004; Cody & Hillenbrand 2010).

Fig. 1 illustrates the observational scenario typically used to constrain the spin evolution models of low-mass stars by showing some of the most complete data sets to date. Period distributions are shown as a function of mass at 3 Myr, in NGC 2264 (Lamm et al. 2005; Venuti et al. 2017), at ∼8 Myr in Upper Sco (USco, Rebull et al. 2018), at 13 Myr in h Per (Moraux et al. 2013), at 110 Myr in the Pleiades (Rebull et al. 2016), at 710 Myr in the Praesepe (Rebull et al. 2017), and at 1 Gyr in NGC 6811 (Curtis et al. 2019). At the earliest stages of star formation, during the protostellar phase, we still have a poor understanding of what determines the stars' initial spin rates

and what are the fundamental physical mechanisms responsible for their angular momentum changes (e.g. White & Hillenbrand 2004; Covey et al. 2005). However, once the stellar photosphere becomes visible, enabling the measurement of spin rates from the rotational modulation of spots at the stellar surface, existing measurements of spin rates in star-forming regions reveal a broad distribution at all masses, with spin rates ranging from a fast rotation close to the break-up limit to slow rotators of about a dozen days (e.g. Irwin & Bouvier 2009; Bouvier et al. 2014).

However, as broad as the initial spin rate distributions are, they soon become highly sub-structured. For example, most of the data sets in Fig. 1 show some level of mass dependence in their period-mass distributions. At the age of 3 Myr, the period-mass distribution of NGC 2264 hints at a dearth of slow rotators among the cluster's lowest mass stars ($\sim$0.2 $M_\odot$), with members under 0.4 $M_\odot$ rotating on average 2.2 d faster than members above this mass, and with no star rotating faster than one day among the highest mass ones. At the age of 8 Myr, the majority of USco members with masses under 0.4 $M_\odot$ are fast rotators, with a trend of faster rotation towards lower masses. This lack of slow rotators among the very low-mass stars is observed in most clusters monitored by campaigns sensitive to these fainter stars.

Once the discs are dissipated and the SDI phase is over, stars become free to spin-up due to their PMS contraction until they reach the zero-age MS (ZAMS) and the ignition of hydrogen takes place. As lower-mass stars take longer to reach the ZAMS, they will spin-up for longer periods of time, partially explaining the strong mass dependence observed at the Pleiades and Praesepe and visible in Fig. 1. However, we still lack an explanation for the mass-dependence observed at the start of the spin-up phase.

During the MS phase, the rotational evolution of stars becomes dominated by the spin-down due to mass-loss via magnetized winds. At later MS ages ($\gtrsim$1 Gyr), the rotation rates of solar-type stars are observed to converge towards a narrow range of rotation rates that decreases approximately as the square root of the age (Skumanich 1972). This convergence happens in a mass-dependent way, i.e. more massive stars converge to the sequence at earlier ages than lower mass stars, and it suggests that the effect of the early stages on the rotational evolution is erased at late ages. The verification of this mass-period-age dependence has given rise to the concept of gyrochronology (Barnes 2003), whereby the rotation rates of stars can be used to constrain ages, which is especially useful during the MS, when other stellar properties are less sensitive to age (Barnes, Spada & Weingrill 2016).

When treated as an evolutionary sequence, the observed distributions of spin rates of different regions can be difficult to reconcile. For example, Coker, Pinsonneault & Terndrup (2016) demonstrated that the observed period-mass distribution at 13 Myr in h Per has an excess of fast-rotating stars that cannot be reproduced by using current spin evolution models to evolve the distribution of the ONC from 1 Myr to h Per's age. Moreover, a recent study by Breimann, Matt & Naylor (2021) suggested that in order to be fitted by current models, present-day observed period-mass distributions of MS clusters require sub-structured initial conditions similar to the period-mass distribution of USco. The origins of both findings may be an environmental influence on the spin evolution of stars and, in parts, motivate this work. In particular, if the PMS environment does indeed influence stellar rotation on $\gtrsim$100 Myr time-scales, stellar rotation can offer a novel probe for the birth environment of stars and their planetary systems and help the investigations of growing claims in the literature for the environmental dependence of planet formation (e.g. Brucalassi et al. 2016; Winter et al. 2020b; Chevance, Kruijssen & Longmore 2021; Longmore, Chevance & Kruijssen 2021; Rodet, Su & Lai 2021).

Working towards a better understanding of how the environment of star formation and early evolution can influence the spin evolution of low-mass stars, we implement the results from a recent model for protoplanetary disc dispersal under the influence of external FUV-photoevaporation by Winter et al. (2020a, hereafter WKC20) into a spin-evolution model that treats the early-PMS phase under the disc-locking hypothesis. We apply this model to investigate the rotational evolution of low mass stars (0.1–1.3 $M_\odot$) from the early-PMS phase to the Sun's age and its dependence on the local FUV environment.

This paper is organized as follows. The implementation of our FUV-irradiated spin evolution model is described in Section 2. In Section 3, we present our results in both rotation-age (Section 3.1) and rotation-mass (Section 3.2) parameter spaces. In Section 3.3, we compare our model results with the statistical properties of the observed period-mass distributions (shown in Fig. 1). In Section 3.4, we add further context to our FUV-dependent spin evolution models by looking at the massive stars' influence on their local-FUV flux. We discuss our model's limitations in Section 4.1 and debate the consequences of the influence of the environment on rotation in Section 4.2. Finally, a summary and conclusions are presented in Section 5.

## 2 MODEL

To explore the role of environmentally induced variable disc dispersal time-scales on the spin evolution of the central star, we require a model for the spin evolution that considers the presence of a disc during the early-PMS phase. Our base spin evolution model follows the general formulation from Matt et al. (2015, hereafter MBB15). In this formulation, the spin evolution of the star is derived by using a forward-time-stepping Euler-method for solving the angular momentum differential equation for given initial conditions:

$$\frac{\mathrm{d}\Omega}{\mathrm{d}t} = \frac{T}{I} - \frac{\Omega}{I}\frac{\mathrm{d}I}{\mathrm{d}t}. \tag{1}$$

Where $\Omega$ is the stellar angular velocity, $I$ is the stellar momentum of inertia, and $T$ represents the torques in action.

Our model is based on three assumptions. First, the stars are considered solid body rotators and their radius, $R_*$, their momentum of inertia, $I$, and its variation with time, $\frac{dI}{dt}$, are interpolated from a standard stellar evolutionary model as in MBB15; however, here we used the updated stellar evolutionary tracks of Baraffe et al. (2015). This solid-body approximation means that any angular momentum exchange with the exterior at the stellar surface is instantaneously communicated to the stellar interior. This approximation represents the limiting case of rapid internal angular momentum transport and neglects any possible effects from internal differential rotation. These limitations are discussed in Section 4.1.3, along with alternative formulations.

The second assumption is the hypothesis of the disc-locking scenario which is discussed and implemented in Section 2.1. The third assumption is that once the disc-locking phase has finished, the only torque in action is the one from magnetized winds. The wind braking law adopted and its implementation are discussed in Section 2.2. Finally, we discussed the adopted initial conditions in Section 2.3.

### 2.1 Disc evolution

The disc-locking hypothesis has been widely adopted by previous models in the literature (e.g. Bouvier et al. 1997; Gallet & Bouvier

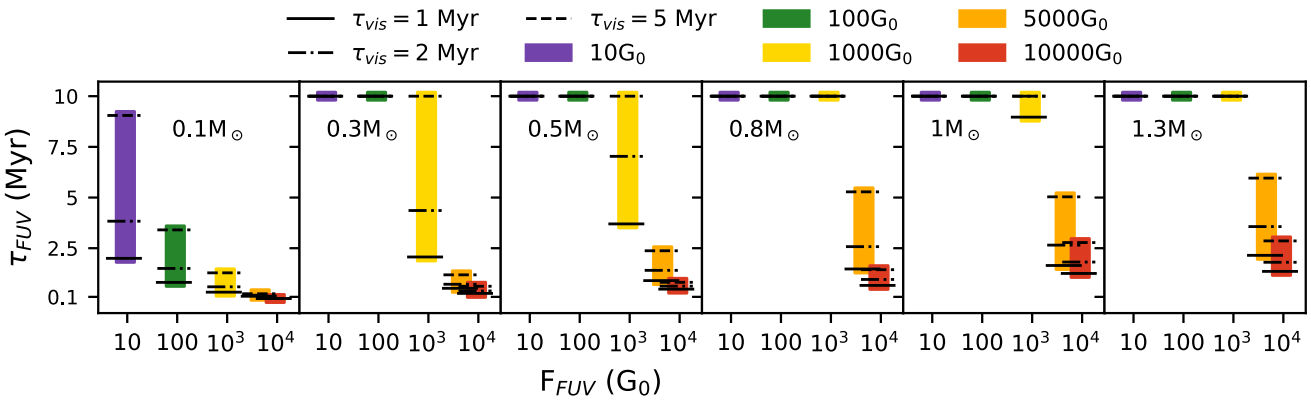


**Figure 2.** Time-scales for dissipation of viscous discs under the influence of external FUV-driven photoevaporation as a function of local FUV fluxes, which were used for constraining the disc-locking phase duration in our model. Results are shown for stellar masses, local FUV flux and viscous time-scales at which models were calculated by WKC20: at 10, 100, 1000, 5000, and 10 000 $G_0$ for stars with 0.1, 0.3, 0.5, 0.8, 1, and 1.3 $M_\odot$ masses, and discs with viscous time-scale of 1, 2, or 5 Myr. Note that the bars are centred at the FUV-level they represent; however, their width is set for visualization purposes only.

2013, 2015; Vasconcelos & Bouvier 2015, 2017; Amard et al. 2016; Landin et al. 2016; Johnstone, Bartel & Güdel 2021) and has the observational support discussed in the Section 1. In this scenario, as a consequence of the magnetic SDI, stars that are still accreting are exchanging angular momentum with their discs, and the net result of this interaction is a torque that counteracts the stellar contraction and stellar winds. Hence, while disc locking is in action,

$$T_{\rm SDI} = \Omega \frac{{\rm d}I}{{\rm d}t} - T_W, \tag{2}$$

and therefore $\frac{{\rm d}\Omega}{{\rm d}t} = 0$. In our model, the star is kept with constant rotation for a time-scale $\tau_{\rm D}$ which will depend on details of the disc evolution process.[1] Alternative formulations for equation (2) exist in the literature, including explicit formulations for the $T_{\rm SDI}$ and treatments for the SDI phase with $\frac{{\rm d}\Omega}{{\rm d}t} \neq 0$. Those are discussed in Section 4.1.1, along with the limitations of the disc-locking hypothesis.

In order to evaluate the duration of the SDI phase, we used results from the viscous-accretion disc dissipation models by WKC20 which considers the evolution of an $\alpha$-disc that is subject to mass-loss due to external photoevaporation at its outer radius and accretion of the material in the inner disc. WKC20 considers a one-dimensional disc evolution as in Clarke (2007), and subsequently Winter et al. (2018), with similar solutions to the disc evolution from Lynden-Bell & Pringle (1974). In this model, the viscosity of the disc scales with its radius, with a scaling radius of 40 au, the mass of the star, $M_*$, and a viscous time-scale $\tau_{\rm vis} \propto \frac{M_{\rm disk}}{\dot{M}_{\rm acc}}$ (see also Winter, Clarke & Rosotti 2019). The disc has an initial mass of $0.1M_*$, which is broadly consistent with the evidence that the initial mass of discs are related to the mass of the host star (e.g. Natta, Grinin & Mannings 2000; Natta, Testi & Randich 2006; Fang et al. 2009; Rigliaco et al. 2011; Williams & Cieza 2011; Andrews et al. 2013; Alcalá et al. 2014; Pascucci et al. 2016; Manara et al. 2017). The disc evolves due to both accretion from the disc on to the star and external photoevaporation of material in the disc's outer edge, with the mass-loss rate due to external photoevaporation interpolated from the FRIED grid (FUV Radiation Induced Evaporation of Discs, Haworth et al. 2018b). Other physical processes expected to give secondary contributions to the dissipation of discs are not included in WKC20 but are discussed in Section 4.1.2.

WKC20 evolved their disc model to derive FUV-induced disc destruction time-scales, $\tau_{\rm FUV}$, calculated as a function of stellar mass, $M_*$, local FUV flux, $F_{\rm FUV}$, and viscosity time-scale, $\tau_{\rm vis}$, with a disc considered dissipated when its mass becomes smaller than $10^{-5}$ $M_\odot$ and with $F_{\rm FUV}$ expressed in terms of Habing flux, $G_0 = 1.6 \times 10^{-3}$ erg cm$^{-2}$ s$^{-1}$ (Habing 1968). $F_{\rm FUV}$ values of 10, 100, 1000, 5000, and 10 000 $G_0$ are considered. These are the values for which the FRIED grid is calculated, and cover the typical range of $F_{\rm FUV}$ expected in clusters (10–$10^6$$G_0$, e.g., Fatuzzo & Adams 2008; Winter et al. 2018). The highest FUV flux considered was $F_{\rm FUV} = 10^4$ $G_0$, with $\tau_{\rm FUV}$ saturating at this value. For larger fluxes than $10^4$ $G_0$, the temperature in the photodissociation of the disc becomes insensitive to the FUV irradiation and the mass flux and thermal winds will remain approximately constant (Hollenbach & Tielens 1997; Johnstone et al. 1998). A minimum disc dissipation time-scale was therefore imposed imposed, with $\tau_{\rm FUV}$ saturating at $10^4$ $G_0$. A maximum time-scale for disc dissipation of 10 Myr was also set, with the argument that if the disc survives external photoevaporation, it would be dissipated in this time-scale due to internal processes.

Results for $\tau_{\rm FUV}$ are plotted as a function of $F_{\rm FUV}$ in Fig. 2 for six masses inside our mass range of interest, 0.1, 0.3, 0.5, 0.8, 1, and 1.3 $M_\odot$. The results are also shown for $\tau_{\rm vis}$ of 1, 2, and 5 Myr. For further reference, the tabulations for $\tau_{\rm FUV}$ as a function of $F_{\rm FUV}$ presented in Fig. 2 are also provided in Table B1 in the Appendix. In the later development of our model we interpolated the appropriate $\tau_{\rm FUV}$ from Fig. 2 for intermediate masses and $F_{\rm FUV}$ values.

At a fixed viscous time-scale, the disc-dissipation model adopted introduces a strong mass dependence on the time-scales of disc dissipation. This mass dependence comes from the FUV-induced mass-loss rates from the FRIED grid, which at a fixed FUV-level are systematically higher for decreasing stellar masses. This happens because lower mass stars have shallower gravitational potentials, and consequently the material in their discs is less bound to the parent star (Haworth et al. 2018b). For higher mass stars, the FUV-radiation is only efficient in photoevaporating the material in the disc down to certain radii that depend on the disc mass, disc viscosity, and on the FUV field strength. Hence, within the disc parameters covered by WKC20, stars with $M_* \geq 0.3$ $M_\odot$ will be insensitive to external photoevaporation under low-FUV levels ($F_{\rm FUV} \leq 100$ $G_0$, purple and green bars in Fig. 2). For lower mass stars with $M_* < 0.3$ $M_\odot$,

[1]Note that in this paper, we use the terms 'disc-locking duration', 'disc dissipation time-scale' and 'disc lifetime' interchangeably.

material in the disc is externally photoevaporated more efficiently and down to smaller radii even under FUV-levels as low as 10 $G_0$. Consequently, for a 0.1 $M_\odot$ star, the maximum $\tau_{FUV}$ is between 2 and 9 Myr, depending on $\tau_{vis}$.

Note that within the parameter space covered by the disc model adopted, some combinations of $F_{FUV}$ and $\tau_{vis}$ yield similar disc-dissipation time-scales. For example, a 1 $M_\odot$ star has its disc dissipated in 2.8 Myr considering both $\tau_{vis} = 1$ Myr with a 4370 $G_0$ FUV level, and a $\tau_{vis} = 5$ Myr with a $10^4$ $G_0$ FUV level. Despite this, Fig. 2 shows that even though this degeneracy diminishes the strength of the mass dependence of the disc-dissipation process for $M_* \geq 0.3$ $M_\odot$ at the largest FUV levels, the overall mass dependence is still significant over the whole 0.1–1.3 $M_\odot$ mass range.

### 2.2 Wind torque

The SDI ceases when the disc is dissipated after a time-scale $\tau_D \approx \tau_{FUV}$, and after that, the only torque acting in the star is the torque from magnetized winds $T_W$. The $T_W$ adopted is the semi-empirically calibrated one of MBB15, which depends on the Rossby number of the stars, $R_0 \equiv \frac{1}{\Omega_* \tau_{cz}}$, and where $\tau_{cz}$ is the convective turnover time-scale:

$$T_W = \begin{cases} T_0 \left(\frac{\tau_{cz}}{\tau_{cz\odot}}\right)^2 \left(\frac{\Omega_*}{\Omega_\odot}\right)^3, & \text{if} \Omega_* \leq 10\Omega_\odot \frac{\tau_{cz\odot}}{\tau_{cz}} \quad \text{(unsaturated)} \\ -100 T_0 \left(\frac{\Omega_*}{\Omega_\odot}\right), & \text{otherwise.} \quad \text{(saturated)} \end{cases} \tag{3}$$

Where the torque scaling, $T_0 = 6.3 \times 10^{30} \text{erg} \left(\frac{R_*}{R_\odot}\right)^{3.1} \left(\frac{M_*}{M_\odot}\right)^{0.5}$, is calibrated to the Sun. At each time-step, $\tau_{cz}$ is computed using the prescription from Cranmer & Saar (2011) based on the star's effective temperature. The limitations of the prescription for $\tau_{cz}$ are discussed in Section 4.1.4. We refer to MBB15 and references therein for a full discussion on the formulation of equation (3). Because we updated the MBB15 models to use the evolutionary tracks of Baraffe et al. (2015), we had to also update the value for $\tau_{cz,\odot}$. This is required because the Baraffe et al. (2015) evolutionary tracks are not calibrated to the Sun, and therefore a 1 $M_\odot$ star at the age of the Sun (4.56 Gyr) will have a slightly different effective temperature from the Sun, of 5716 K, and $\tau_{cz,\odot} = 13.8$ d.

Finally, the rotational break-up limit is estimated as

$$\Omega_{breakup} = \sqrt{\frac{GM_*}{(1.5R_*)^3}}, \tag{4}$$

following Maeder (2009, Chapter 2). At spin rates close to this break-up limit, the material at the stellar equator becomes gravitationally unbound, which can induce augmented mass-loss rates and stellar wind geometry that differ from those in the wind-torque prescription adopted in this study. It is beyond the scope of this paper to explore how the torque would change close to break-up limit. Instead, we introduce a saturation condition in the spin-up phase, where stars are prevented from spinning faster than the break-up limit set by equation (4). Whilst this is an oversimplification of the physics involved, it is effectively the same as assuming that stars rotating close to the break-up limit would have stronger wind torques that would efficiently brake them down, preventing them from rotating faster than the break-up limit. This assumption is required because, as presented in Fig. 2 and later discussed in this paper, under the highest FUV fluxes considered, the disc-locking duration can be significantly shortened even for the higher mass stars, leading to very long spin-up phases that, otherwise, would result in stars exceeding the break-up limit.

### 2.3 Initial conditions

The lifetime of Class 0/I young stellar objects is estimated to be about 0.5 Myr (Evans et al. 2009). Hence, by starting our model after this phase, we can assume that the stars are past the phase of high and episodic accretion observed in Class I objects (e.g. Herbig 1977; Audard et al. 2014; Hartmann, Herczeg & Calvet 2016), and therefore their disc evolution is well approached by the model described in Section 2.1. Conveniently, the youngest age available for the whole 0.1–1.3 $M_\odot$ mass range in Baraffe et al. (2015)'s evolutionary tracks is 0.55 Myr, which is our starting point.

At 0.55 Myr, we do not have direct observations for the period distributions. Instead, we based our choice of initial rotation rate on the earliest aged clusters observed like Taurus and $\rho$Oph ($\lesssim$3 Myr; Rebull et al. 2018, 2020), the ONC ($\lesssim$3 Myr; Rodríguez-Ledesma, Mundt & Eislöffel 2009), and NGC 2264 ($\sim$3 Myr; Venuti et al. 2017), which exhibit broad period distributions from $\sim$16 d down to close to the break-up limit. While working under the disc-locking hypothesis, the range of rotation rates observed in disc-bearing stars during the PMS should reflect the range of initial rotation rates at the age of 0.55 Myr. For example, when considering the observed spin rates in $\rho$Oph, USco and Taurus, which are the closest young regions observed ($\lesssim$140 pc) and therefore have very complete samples of very-low mass stars, the majority of disc-bearing stars at all masses have rotation periods of about 1.6 d or larger. Motivated by that, we considered two extreme values as initial conditions: a fastest initial spin rate of 1.6 d sets the minimum initial rotational period considered. This minimum value is compatible with the break-up limit at 0.55 Myr, which varies between 0.7 and 1.2 d depending on the stellar mass. For the maximum initial rotational period, we adopted the slowest rotation of 16 d, which reflects the maximum rotation rates typically observed in young regions.

In Fig. 2, some of the lower mass stars evolving under high FUV fluxes have their disc dissipated earlier than the age at which we start our model. For example, a 0.1 $M_\odot$ star evolving under 10 000 $G_0$ has its disc dissipated in 19 000 yr resulting in 0.53 Myr of spin-up before the beginning of our spin evolution model at 0.55 Myr. This means that our initial conditions, which are based on the rotational properties of disc-bearing stars, might be too slow for such stars. However, these are also the models that reach the break-up limit during their spin-up phase. Therefore, enforcing faster initial conditions for those would only induce an earlier saturation of their rotation at the break-up limit.

## 3 RESULTS

### 3.1 FUV irradiated spin evolution

Fig. 3 shows the results of the FUV irradiated spin-evolution model described in Section 2, presented here with rotation rate as a function of stellar age. The models presented in Fig. 3 are run using the two limit initial rotation rates discussed in Section 2.3 (1.6 and 16 d), for each mass (0.1, 0.3, 0.5, 0.8, 1, and 1.3 $M_\odot$), local FUV flux (10, 100, 1000, 5000, and 10 000$G_0$), and $\tau_{vis}$ (1, 2, and 5 Myr) for which the disc-dissipation time-scales were estimated in Section 2.1.

#### *3.1.1 Overall trends*

The general trend seen in Fig. 3 is that stars significantly affected by external photoevaporation are released from their discs earlier, having a reduced disc-locking duration. Consequently, these stars

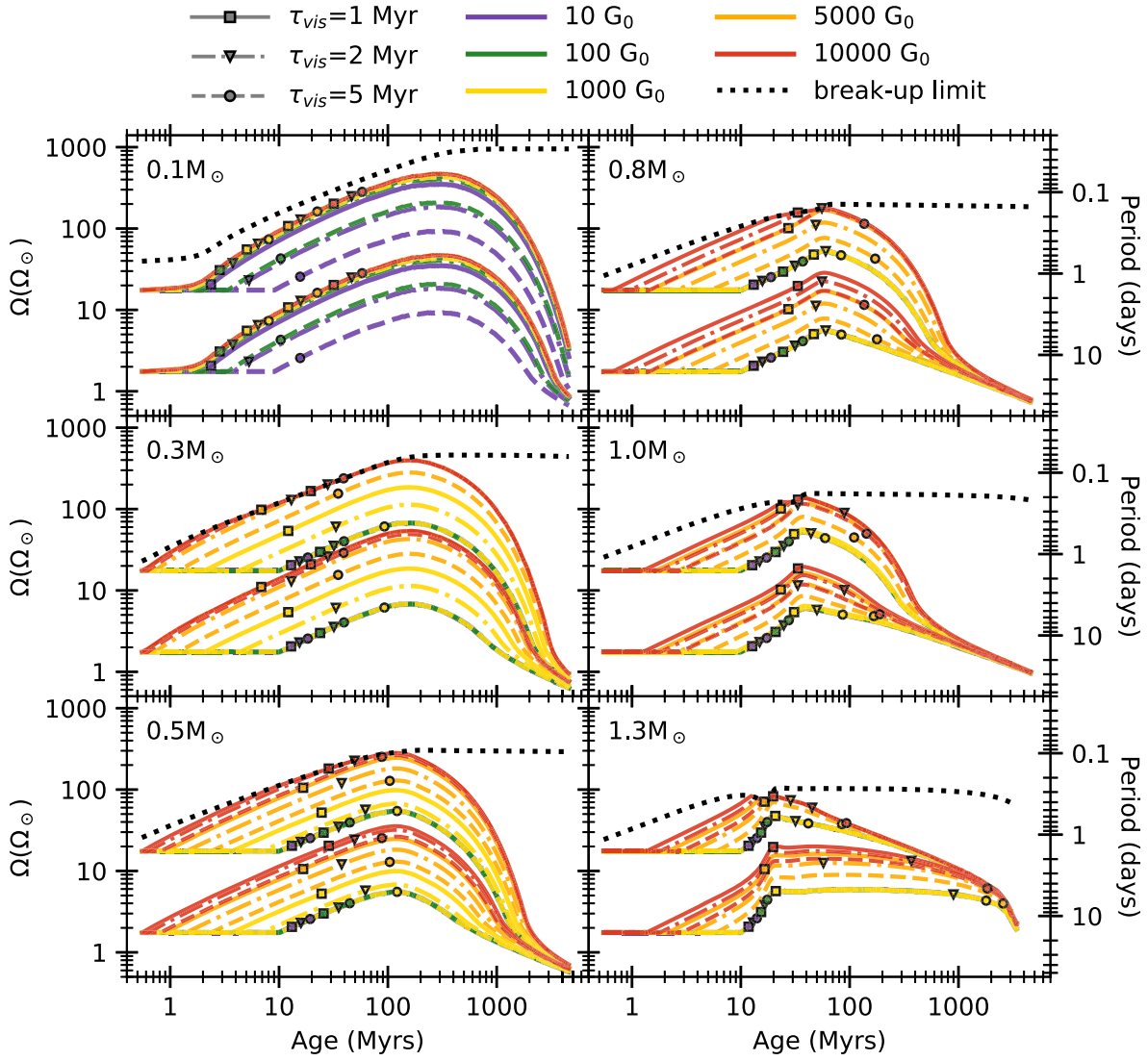


**Figure 3.** FUV-irradiated spin evolution models for stars with 0.1, 0.3, 0.5, 0.8, 1, and 1.3 $M_{\odot}$. The purple, green, yellow, orange and red lines present models for local FUV fluxes of 10, 100, 1000, 5000, and 10 000$G_0$ respectively. Models for initial rotation rates of 1.6 and 16 d are shown. Continuous, dashed, and dash–dotted lines show the models for $\tau_{\rm vis}$ of 1, 2, and 5 Myr, respectively. In order to facilitate the visualization of models that fall on top of each other, a full squared, triangle or circle symbol is plotted at an arbitrary position for $\tau_{\rm vis}$ of 1, 2, and 5 Myr, respectively. The dashed black line shows the critical rotation limit for each mass.

have a longer spin-up phase and reach the ZAMS rotating faster than stars with the same mass, viscous time-scale, and initial condition but unaffected by external photoevaporation.

### *3.1.2 Disc viscosity dependence*

At a fixed mass and FUV flux, the disc-locking duration of stars having discs with shorter viscous time-scales are more strongly reduced by external photoevaporation, as illustrated in Figs 2 and 3. This happens because the disc viscosity influences both the accretion rate and the expansion of the disc into a region where external photoevaporation is efficient (see Winter et al. 2019). Consequently, shorter viscous time-scales generally result in higher accretion rates along with higher mass-loss rates due to external photoevaporation and systematically shorter disc-locking duration. Accordingly, at ages past the SDI, stars that had discs with lower viscous time-scales tend to be faster rotators than stars that had larger viscous time-scale. However, this trend is only seen at specific combinations of stellar mass and FUV irradiation, as discussed in the following sections.

### *3.1.3 Solar-type stars*

Considering stars with $M_{*} \geq 0.3$ $M_{\odot}$, with the same viscous time-scale, and under the same FUV flux, the effect of external photoevaporation will generally result in a shorter disc-locking duration for lower mass stars, and, consequently, at ages past the disc-locking phase, lower mass stars are systematically faster rotators. The only exception is the model for 1 $M_{\odot}$ stars with $\tau_{\rm vis} = 1$ Myr, which has a disc dissipation time-scale $\sim$1 Myr shorter than the 0.8 $M_{\odot}$ star with the same viscous time-scale. This variation is inherited from the FRIED grid (see fig. A3 in Haworth et al. 2018b), which, as the disc evolves and its mass reduces to less than $10^{-4}$ $M_{\odot}$, gives higher mass-loss rates for the 1 $M_{\odot}$ star than the 0.8 $M_{\odot}$, resulting in a quicker disc-dissipation for the former. Consequently, for $\tau_{\rm vis}$

=1 Myr models, 1 $M_\odot$ stars will reach the age of h Per rotating about 10 per cent faster than 0.8 $M_\odot$ stars.

Under low FUV fluxes of 10 and 100 $G_0$ (purple and green lines), all $M_* \geq 0.3$ $M_\odot$ models are unaffected by external photoevaporation regardless of their viscous time-scale. Under an intermediate FUV flux of 1000 $G_0$ (yellow lines), models for 0.3 and 0.5 $M_\odot$ with $\tau_{vis}$ = 5 Myr, and models for masses larger or equal 0.8 $M_\odot$ are also not significantly affected by external photoevaporation, but models for 0.3 and 0.5 $M_\odot$, and $\tau_{vis}$ = 1 and 2 Myr have their disc-locking phase significantly shortened. All the stars are affected when under high FUV fluxes such as 5000 or 10 000 $G_0$ (orange and red lines).

#### 3.1.4 Very low-mass stars

Results for the 0.1 $M_\odot$ models show a distinct behaviour. During the early PMS, when the protostellar centre reaches a temperature of the order of $10^6$ K, the star is fuelled by deuterium burning through the reaction $^2H(p, \gamma)^3He$. The released nuclear energy is able to temporarily halt or at least slow down the contraction of the star. As it is sensitive to the central temperature, this phenomenon happens later for lower mass stars. In the case of the 0.1 $M_\odot$ star model, this stalling can last for more than a million years, during which the stellar radius barely changes, and so does its moment of inertia since the star is fully convective. For 0.1 $M_\odot$ stars evolving under 10 $G_0$, or 0.1 $M_\odot$ stars with $\tau_{vis}$ = 5 Myr discs evolving under 100 $G_0$, the deuterium-burning phase happens while the star is still locked to its disc. However, for all the remaining 0.1 $M_\odot$ models, the disc is dissipated between 19 000 yr and 1.5 Myr, i.e., before the deuterium burning phase is over. Consequently, regardless of the disc being dissipated, 0.1 $M_\odot$ stars retain an approximately constant rotation rate until about 1.5 Myr of evolution, resulting in the overlapping 0.1 $M_\odot$ rotation models seen in Fig. 3.

#### 3.1.5 Saturation at the break-up limit

As a result of our model having a spin-up phase that saturates at the break-up limit (equation 4), some of the highest FUV flux models will converge to a similar spin evolution once they approach their break-up limit. For stars with masses $M \geq 0.8$ $M_\odot$, this happens a few million years before the ZAMS. For the lower mass stars, when this convergence happens, it occurs significantly before the ZAMS. Note, however, that this convergence is an artefact of our model assumptions at extreme parameters and does not necessarily reflect a physical phenomenon (see discussion in Section 4.1.3).

### 3.2 Spin evolution in period-mass space

Next, it is relevant to discuss the stellar mass dependence of rotation in our model in the context of period-mass diagrams, as this is the preferred parameter space for observational studies. For that, we defined 'isogyrochrones', which are tracks that cover the whole mass range modelled and show the spin rates for stars at a certain age, given a common initial condition, $\tau_{vis}$, and local FUV flux. These tracks were estimated using a grid of masses between 0.1 and 1.3 $M_\odot$ sampled in steps of 0.02 $M_\odot$. For each FUV flux (10, 100, 1000, 5000, and 10 000 $G_0$) and viscous time-scale (1, 2, and 5 Myr), we defined a pair of fast and slow isogyrochrones with initial rotation of 1.6 and 16 d, which are aimed at describing the fast- and slow-rotation envelopes of the period-mass distributions.

The results are shown in Fig. 4 at the ages 0.55, 3, 8, 13, 110, 710, 1000, and 4500 Myr. While the initial age is simply the initial age of the evolutionary tracks of Baraffe et al. (2015), discussed in Section 2.3, the subsequent ages shown are the approximate ages of the data sets in Fig. 1 – NGC 2264, USco, h Per, Pleiades, Praesepe, NGC 6811 – and the Sun, respectively. For improving the visualization, we omitted the 100 $G_0$ models from Fig. 4, as the models for 100 $G_0$ with $\tau_{vis}$=1 and 2 Myr were very similar to the 10 $G_0$, $\tau_{vis}$=1 Myr model and the 100 $G_0$, $\tau_{vis}$ = 5 Myr model was very similar to the 10 $G_0$ $\tau_{vis}$ = 2 Myr model. Models for 100 $G_0$ with $\tau_{vis}$=1 Myr are later shown in Fig. 5.

#### 3.2.1 Control case: no external photoevaporation

For comparison, we also analysed a control case without external photoevaporation. For that, we considered a pair of isogyrochrones with initial rotation of 1.6 and 16 d and a fixed disc-locking duration of 5 Myr at all masses, which is equivalent to the MBB15 model but revised under the disc-locking hypothesis. This control case is presented as bold black lines in Fig. 4.

The isogyrochrones for the control case illustrate how, without external photoevaporation, the spin evolution only becomes mass-dependent close to the age of the Pleiades. This late mass dependence is also present in the spin evolution with external photoevaporation as it is inherent to MBB15 wind torque (see equation 3, Section 2.2), which has a dependence on stellar mass ($M_*$) and radius ($R_*$), and on the convective turnover time-scale ($\tau_{cz}$, which in turn depends on the effective temperature of the star). However, the mass dependence introduced by the MBB15 torque only become evident at MS ages, when the spin evolution of stars is dominated by the wind-torque. Hence, the control case isogyrochrones in Fig. 4 illustrates how without external photoevaporation the period distributions of young stars ($\lesssim$15 Myr) are independent of stellar mass, which is inconsistent with the observed period-mass distributions at the age of NGC 2264 and USco (see also Figs 1 and 5).

#### 3.2.2 Trends for FUV-irradiated discs

In contrast to the control case, all FUV-irradiated isogyrochrones are mass-dependent since the early PMS phase, with the 10 $G_0$ model with $\tau_{vis}$ = 5 Myr as the only exception. This dependence is independent of the initial rotation. Hence, this is visible in both the fast and slow isogyrochrones, with a dearth of slowest rotators and an excess of faster rotators among the lowest mass stars. This feature is explained by the significant stellar mass dependence of the external photoevaporation of discs and its contribution to the disc-dissipation process, discussed in Section 2.1, which under any fixed FUV flux results in an earlier start of the PMS spin-up phase for lower mass stars. Accordingly, Figs 2 and 4 illustrate how the stellar mass dependence in the dissipation of FUV-irradiated discs translates into a mass-dependent PMS rotational evolution. A careful comparison between the two figures reveals a time-lag between a star being released from its disc and this resulting in a spin-up significant enough to be visible in the period-mass space. For example, 1 $M_\odot$ stars evolving under an FUV irradiation of 10 000 $G_0$ lose their discs in 1.3, 1.8, and 2.8 Myr for $\tau_{vis}$ of 1, 2, and 5 Myr, respectively. Accordingly, at 3 Myr, the stars with a $\tau_{vis}$ of 1 and 2 Myr already had 1.7 and 1.2 Myr to spin-up, respectively, and have reached spin rates of 9 and 11.5 d. Meanwhile, the star with $\tau_{vis}$=5 Myr just recently started spinning up, having a spin rate of 15.3 d, which is indistinguishable from its 16 d initial rotation within the typical precision of rotational surveys. This time lag is probably the explanation for the existence of slow-rotating discless stars in

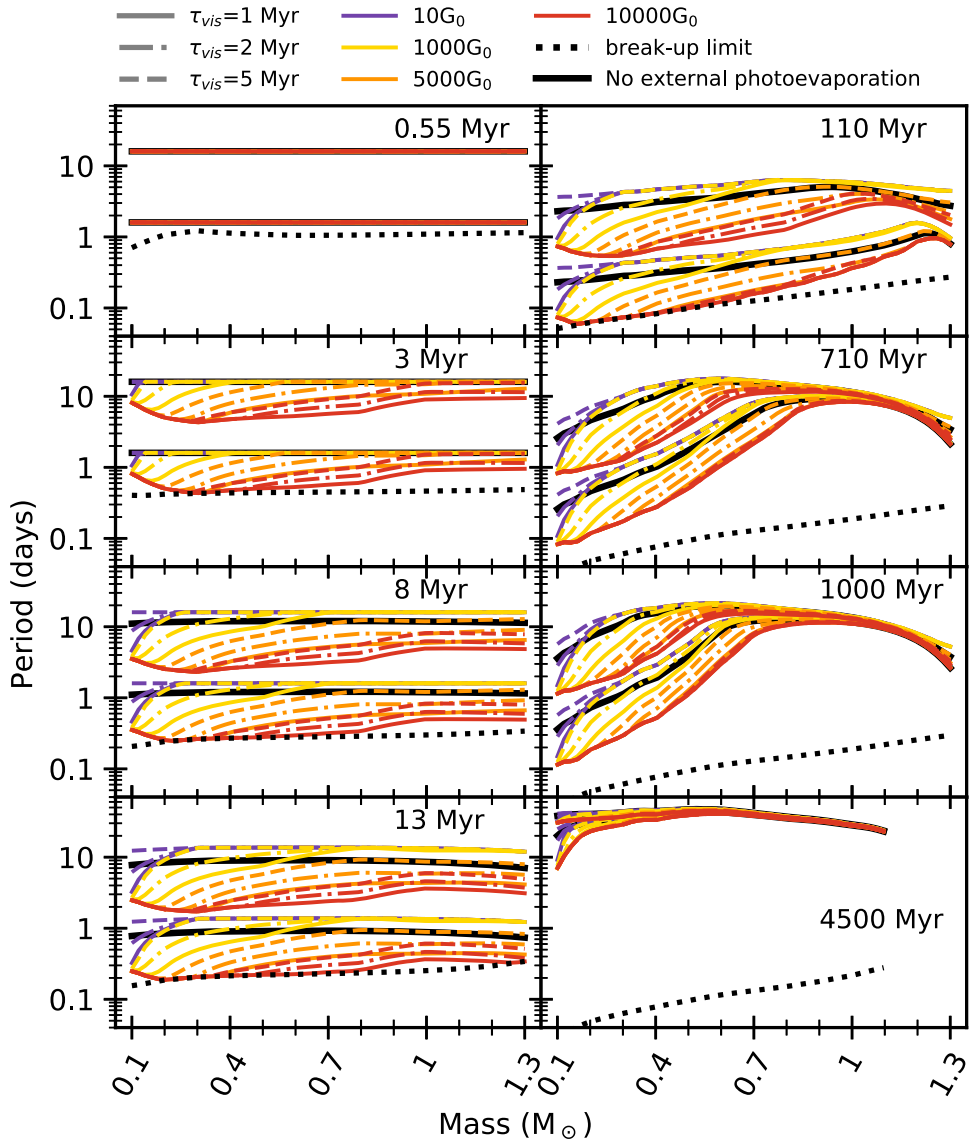


**Figure 4.** FUV-irradiated spin evolution model results in the period-mass space. Coloured lines show isogyrochrones for models at four different FUV fluxes: 10 $G_0$ (purple), 1000 $G_0$ (yellow), 5000 $G_0$ (orange), and 10 000 $G_0$ (red). At each FUV-level, models are presented for three values of viscous time-scale: $\tau_{vis}$ =1 Myr (continuous lines), $\tau_{vis}$ = 2 Myr (dash–dotted lines), and $\tau_{vis}$ = 5 Myr (dashed lines). Each pair of isogyrochrones are for initial conditions with slow-rotation of 16 d (top lines) and fast-rotation of 1.6 d (bottom lines). For comparison, the black-continuous lines shows a model without the influence of external photoevaporation, with a fixed disc-locking duration of 5 Myr and independent of the properties of the stars. Models start at 0.55 Myr and are evolved until the age of the Sun (4.5 Gyr), with snapshots shown at the ages of NGC 2264 (3 Myr), USco (8 Myr), h Per (13 Myr), Pleiades (110 Myr), Praesepe (710 Myr), and NGC 6811 (1 Gyr). The break-up limit at each age is shown as a dotted black line. Isogyrochrones for the FUV flux of 100 $G_0$ are omitted from this plot, as they are very similar to the 10 $G_0$ models.

some of the youngest regions observed (e.g. NGC 2264; Venuti et al. 2017).

The local FUV irradiation also dictates how early this mass dependence is present in the period-mass diagram. Under intermediate and high FUV fluxes, this mass dependence is already present at ages as early as 3 Myr. The mass range in which this mass dependence is present increases through the early-PMS, and it is maximum at a few million years after stars at all masses and FUV fluxes have lost their discs. The extent of this mass dependence increases with FUV flux until intermediate levels. At low FUV fluxes, discs are only mildly influenced by external photoevaporation, while under the highest FUV fluxes, all discs are quickly destroyed. In these extremes, discs under similar FUV fluxes have broadly similar disc-locking duration, and the resultant differences in rotation rates are relatively small. However, under intermediate FUV fluxes, the variations of external photoevaporation mass-loss rates as a function of stellar mass are large, so the beginning of the spin-up phase varies strongly between stars of different masses. For example, considering the $\tau_{vis}$ = 1 Myr models, the ratio between the spin rate of a 1 $M_\odot$ and a 0.2 $M_\odot$ star by the age of h Per (13 Myr) is 1.4, 4.4, and 1.9 under FUV-fluxes of 10, 1000, and 10 000 $G_0$, respectively.

Finally, the mass dependence in our models remain visible in the period-mass space even past the ZAMS, and it only disappears later on the MS, when higher mass stars start converging to a single

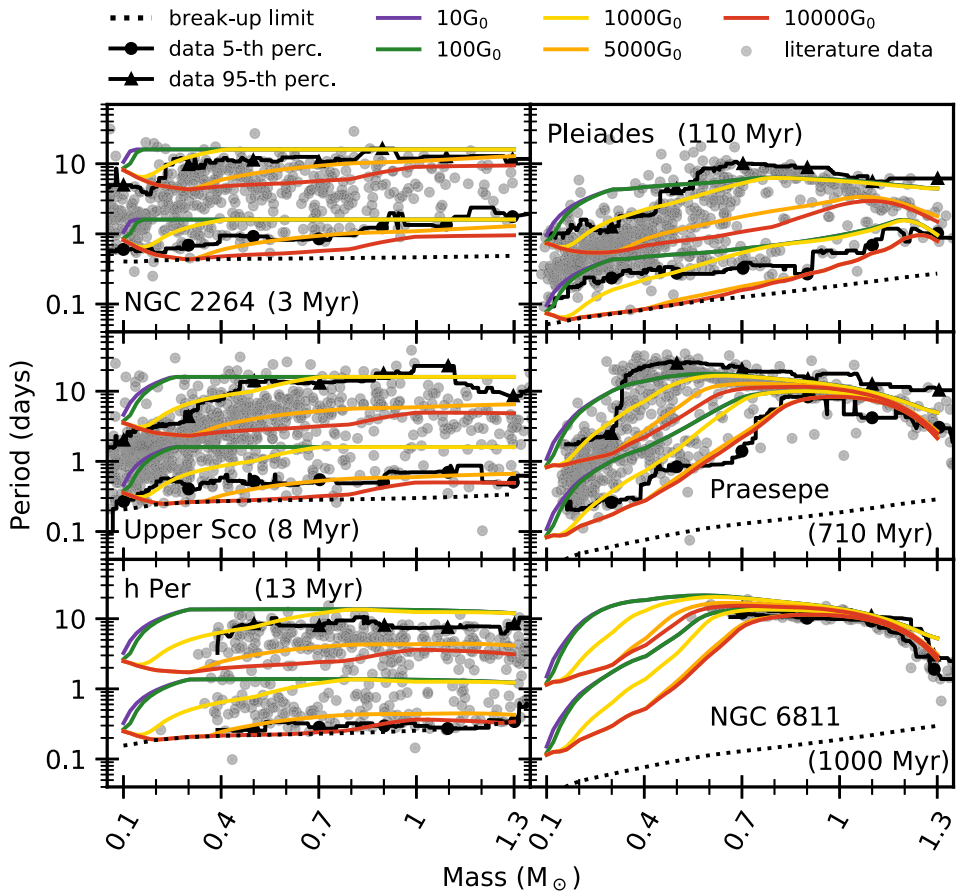


**Figure 5.** Observed period-mass distributions for NGC 2264, USco, h Per, Pleiades, Praesepe and NGC 6811, presented along with the isogyrochrones for models with $\tau_{\rm vis}$ =1 Myr at different FUV-fluxes and at the age of each cluster, with the 5th and 95th rolling percentiles of these distributions overplotted as in Fig. 1. Rolling-percentiles are calculated similarly to moving-averages, where the period-mass distributions are ordered as a function of ascending mass, with the percentile at a given mass estimated from a subset of observations around that mass, using subset sizes between 5 and 15 per cent of the total number of stars in that observed data set.

slow-rotating sequence. Notably, while having longer spin-up phases, high-FUV models also have longer spin-down phases, such that, at a fixed age, the minimum mass at which the models converged to the slow sequence depends on the FUV irradiation of the model.

### 3.3 Comparing models to observed period-mass distributions

Fig. 5 shows the isogyrochrones for $\tau_{\rm vis} = 1$ Myr, discussed in the previous section, overplotted to the observed data sets. As in Fig. 1, we present observed data sets along with the rolling-percentiles of these period-mass distributions, with the 5th and 95th percentile describing the distribution's fast and slow rotating envelopes and being comparable to the fast and slow isogyrochrones, respectively. We stress that this comparison is not aimed at reproducing the details of the substructures observed within these period-mass distributions, which would demand more detailed modelling of the initial distribution of spin rates and is beyond our scope.

The general trend seen in Fig. 5 is that no model for single FUV flux can simultaneously explain both the 5th and 95th percentiles of observed clusters, indicating that to reproduce the statistical properties of observed period-mass distributions in clusters, prior knowledge of the distributions of FUV-fluxes within PMS clusters may be required. As the 5th percentiles of most clusters are better approached by higher FUV fast-isogyrochrones, while the 95th percentiles are better approached by intermediate to low FUV slow isogyrochrones, a scenario emerges in which the fast-rotating population of clusters seem to be composed by stars that have evolved under high-FUV fluxes within a cluster, while the slow-rotating population has evolved under lower FUV fluxes. Accordingly, the outliers to the period-mass distributions can be explained as sources evolving under FUV-levels that diverge from the bulk of FUV-fluxes within a cluster. The scenario of a distribution of FUV-fluxes is further explored in Section 3.4.

#### *3.3.1 Early-PMS (≲15 Myr) regions*

At 3 Myr, NGC 2264 period-mass distribution has a dearth of slow rotators among the stars with $M_* \leq 0.3$ M$_\odot$, which is extended to $M_* \leq 0.5$ M$_\odot$ by the age of USco. Fig. 5 shows that this behaviour can be reproduced by intermediate-FUV models, with the shape of the 1000 G$_0$ slow-isogyrochrone approximately reflecting both NGC 2264 and USco slow rotators. In particular, we note that the 95th rolling-percentile of USco reveals a period-mass dependence on the contrary sense for $M_* \gtrsim 1$ M$_\odot$, with higher mass stars rotating faster than solar mass stars – previously noticed by Rebull et al. (2018) – which our models are unable to reproduce (see discussion in Section 4.1.2). At 13 Myr, the lack of observations for stars with $M_* \leq 0.4$ M$_\odot$ in h Per hampers the comparison of its rotational distribution

with the isogyrochrones for different FUV. Nevertheless, h Per slow rotators shows intermediate properties between the 1000 $G_0$ and the 5000 $G_0$ slow isogyrochrones.

The shapes of the 5th rolling-percentile in the three younger regions are generally consistent with the shape of the highest FUV fast isogyrochrones, and in the case of NGC 2264, our high-FUV models correctly reproduce the lack of stars rotating faster than 1 d among NGC 2264 stars with $M_* \gtrsim 0.9$ $M_\odot$. However, while at h Per's age, the 10 000 $G_0$ fast-isogyrochrone reflects the location of h Per's 5th rolling percentile, in the case of NGC 2264 and USco, the initial condition of 1.6 d results in isogyrochrones too fast for describing the bulk of these region's fast rotators. Similarly, starting from the initial condition of 16 d allows reproducing the location of the slow-rotation envelope in USco, but results in a slow-isogyrochrone about 4 d too slow for NGC 2264.

#### *3.3.2 MS regions ($\gtrsim$100 Myr)*

At later ages, the shapes of our isogyrochrones are less well matched to the observation's percentiles, which is due to a combination of missing physics in our model – specially regarding our solid-body assumption (see discussion in Section 4.1.3) – and our simplified assumptions regarding the initial distributions of spin rates and single local FUV fluxes. Nevertheless, some of the general properties of the MS regions' period-mass distributions can still be approached by our models.

For example, at the age of the Pleiades (110 Myr), the mass dependence in the 95th percentile is well described by the 1000$G_0$ isogyrochrone over the mass-range $M_* \lesssim 0.5$ $M_\odot$. On the other hand, the 5th percentile has intermediate properties between the intermediate and high-FUV models. By the age of Praesepe (710 Myr), the higher mass solar-type stars ($M_* \gtrsim 0.9$ $M_\odot$) are already converging to a narrow sequence of slow rotation. As the MBB15 model was tuned to fit the Praesepe cluster, all isogyrochrones converge to reproduce the cluster's slow-sequence at Praesepe age. As discussed in Section 1, this convergence happens in a mass-dependent way, and it means that the initial conditions – including the ones induced by the environment – are erased from the period-mass diagram. Nevertheless, as noted in Section 3.2, at a fixed age, the lowest mass at which some of the stars have started to converge to the slow-sequence will depend on both the initial conditions and on the local FUV fluxes. The faster the star's rotation is at the end of the PMS contraction phase, the longer it will take for the star to spin-down under the torque of magnetized winds. As stars under the highest FUV levels will have longer spin-up phases, these will be the last ones to converge to the slow-sequence, and therefore the fingerprint of the initial conditions of stars submitted to higher local FUV flux during the PMS phase will be visible in the period-mass distributions for longer, which suggests that at a given mass and age, fast rotation rates for stars younger than a few Gyr could potentially work as a link between MS stars and their birth environment (see discussion in Section 4.2.4). Finally, by the age of NGC 6811, even though a significant mass range already converged to the slow sequence, the converged isogyrochrones seem to rotate on average slower than the observed data, indicating that the models of MBB15 need further modification (e.g. to the external torque or to relax the assumption of solid-body rotation).

### 3.4 The neighbourhood of massive stars

As discussed in the previous section, the mass-FUV-dependent disc-dissipation models introduced in our spin evolution code greatly

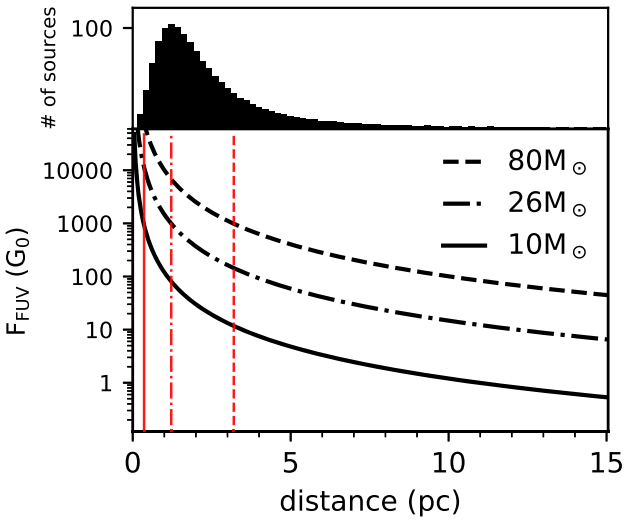


**Figure 6.** Bottom: FUV flux variations in the proximity of three massive stars with 80 $M_\odot$ (dashed line), 26 $M_\odot$ (dash–dotted line), and 10 $M_\odot$ (continuous line). Local FUV fluxes are plotted as a function of distance from the massive stars in parsecs (black lines), while the vertical red lines show the distance at which each star contributes in 1000 $G_0$ to their local flux. Top: The histogram shows the distribution of 1392 sources in a Plummer sphere with a scaling radius of 1.5 pc and central density of 100 sources per $pc^3$, which was used for simulating the evolution of low-mass stars in the neighbourhood of the massive stars in the plot.

contribute to explaining several features observed in the period-mass distributions of open clusters. However, Fig. 5 shows that none of the models for a single FUV-level could simultaneously explain both the 5th and 95th rolling percentiles of the distributions and the outliers. This is not a surprise, as we do not expect the FUV environment of open clusters and star-forming regions to be described by a single FUV flux. At this point, it is useful to add context to the influence of massive stars on their local environment. For that, Fig. 6 portrays the influence of three massive stars with 80, 26, and 10 $M_\odot$ to their local FUV radiation field, where $F_{\rm FUV} = \frac{L_{\rm FUV}(M_*)}{4\pi r^2}$ is the local-FUV flux of a star with mass $M_*$ and FUV luminosity $L_{\rm FUV}(M_*)$, calculated at a distance $r$ from the star. We adopt stellar mass-dependent FUV luminosities as estimated as estimated by Parravano, Hollenbach & McKee (2003), by integrating the stellar flux in the FUV bands using synthetic spectra and Padova models (Bertelli et al. 1994), and averaging the values through the MS lifetime of a massive star. Fig. 6 shows the contribution of massive stars to their FUV environment as a function of distance from the massive stars, and illustrates how this contribution is extremely mass dependent. To facilitate the comparison, the vertical lines show the distance from the massive star where their local FUV flux will be increased by 1000 $G_0$. This is at a distance of 3.20, 1.22, and 0.36 pc for stars with 80, 26, and 10 $M_\odot$, respectively.

To examine the effect of massive stars on the rotational history of low mass stars in their surroundings, we considered the spin evolution of samples of low mass stars spatially distributed in a Plummer sphere (Plummer 1911) around each of the three massive stars in Fig. 6. The distribution of sources in this Plummer sphere is set by

$$\rho(r) = \frac{3N}{4\pi a^3}\left(1+\frac{r^2}{a^2}\right)^{-\frac{5}{2}}, \quad (5)$$

where $N$ is the total number of sources considered, $r$ is the distance to the centre of the sphere, and $a$ is a scaling radius. The Plummer

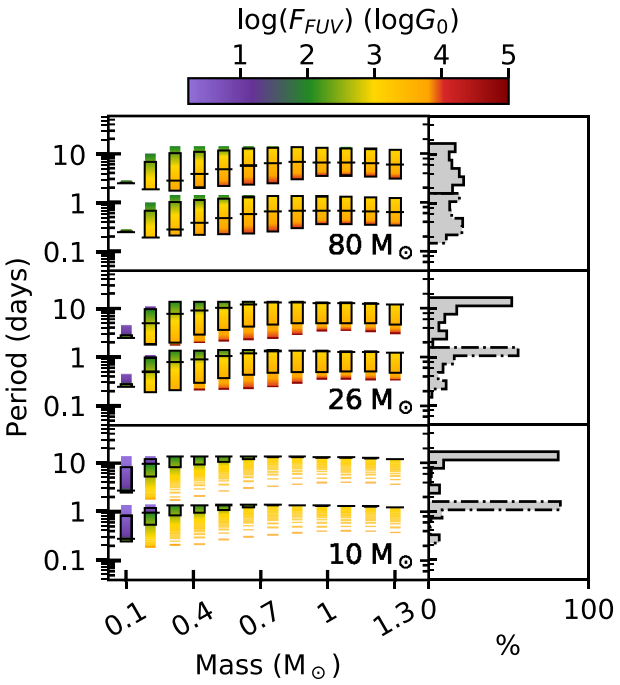


**Figure 7.** Period distributions at 13 Myr for stars evolving around the massive stars shown in Fig. 6, with 80 $M_\odot$ (top), 26 $M_\odot$ (middle), and 10 $M_\odot$ (bottom panels). Left-hand panels show the period distributions of samples of 1392 equal-mass stars distributed in a Plummer sphere around each massive star considering the fast and slow initial conditions of 1.6 and 16 d. Data points ('-' symbols) are coloured by the local FUV-flux at their position [log ($F_{FUV}$)] around the massive star. The box-plots show the 95th (top horizontal line-segment), 50th (middle horizontal line-segment), and 5th percentiles (bottom horizontal line-segment) of the period distribution at each mass and initial condition. Right-hand panels show histograms with the period distributions for the total of 16 704 stars simulated at all masses for the fast (continuous line) and slow (dash–dotted line) initial conditions.

sphere considered has a scaling radius of $a = 1.5$ pc, a central density of 100 stars per pc$^3$, and was truncated at a radius of 15 pc, which is the maximum distance considered in Fig. 6. The distribution of sources in this Plummer sphere is shown in the histogram on the top of Fig. 6. Local-FUV fluxes were estimated at each position based on the central massive star's FUV luminosity and the distance of each source to this central star. This distribution results in samples with 1392 sources evolving under FUV-fluxes in the range of 45–558 682 $G_0$, 7–81 730 $G_0$, and 1–6652 $G_0$ around the 80, 26, and 10$M_\odot$ stars, respectively. The median FUV fluxes were 2695 $G_0$ for the 80$M_\odot$ star, 394 $G_0$ for the 26$M_\odot$, and 3 $G_0$ for the 10$M_\odot$.

Next, considering stellar masses in the range of 0.1–1.3 $M_\odot$ and using steps of 0.1 $M_\odot$, we placed same-mass stars at each of the 1392 positions in the Plummer sphere and modelled their spin evolution. The local FUV-flux at each position were used along with stellar masses and a fixed $\tau_{vis} = 1$ Myr to constrain their disc dissipation time-scales, which were then used as an input to model the spin evolution of these stars. Models were run for fast and slow initial rotation rates of 1.6 or 16 d. Results of their spin evolution are presented in Fig. 7, where we show the period distributions for each mass considered at the age of h Per (13 Myr). We point the reader to Section 4.1.5 for a discussion of the limitations of the model.

Fig. 7 shows that the high-FUV environment of massive stars can skew the period distributions of low mass stars towards faster rotation. Within the context of the toy-model developed in this section, increasing the mass of the massive star at the centre of the Plummer sphere enhances the mass-dependence seen in the period distributions by extending the distribution's mass dependence over a wider mass range and resulting in a lower mass population rotating faster on average than around lower-mass massive stars.

## 4 DISCUSSION

### 4.1 Limitations in the model

#### *4.1.1 Disc-locking hypothesis*

In Section 2.1, equation (2) illustrated how we introduced the disc-locking hypothesis to our models, where the torques involved in the SDI, $T_{SDI}$, counteract the wind-torque and PMS contraction, holding the stellar rotation constant during this interaction. While the same approach has been widely used in the literature, the disc-locking hypothesis is, in truth, an *ad hoc* assumption meant to enforce the lack of spin-up in disc-bearing stars observed during the early-PMS phase while avoiding introducing the large uncertainties in the current theory for the SDI into the spin evolution models. In practice, equation (2) assumes that as the star contracts and its momentum of inertia changes, $T_{SDI}$ will adjust itself in order to counteract this change and keep the rotation rate constant. Hence by setting the initial rotation rates as a free parameter in our model and looking at models with the initial rotation rates of 1.6 and 16 d, we are effectively looking at the extreme values of a range of possible $T_{SDI}$.

A variety of physical mechanisms proposed in the literature could be part of $T_{SDI}$. These are described by numerical models investigating the mechanisms of angular momentum transport during the SDI phase (e.g. Collier Cameron & Campbell 1993; Yi 1994; Armitage & Clarke 1996; Matt et al. 2010) as, for example, X-winds (Shu et al. 1994), accretion-powered stellar winds (Matt et al. 2012), and magnetospheric ejections (Zanni & Ferreira 2013; Gallet, Zanni & Amard 2019). Alternatively, a study by Bouvier & Cébron (2015) also tried to account for the flux of angular momentum involved in the tidal and magnetic interactions between a 1 $M_\odot$ protostar and planets formed in its circumstellar disc. Yet, the majority of these models fail in predicting constant spin rates during the SDI phase, except under unrealistic physical conditions.

While none of these numerical models can currently simultaneously grasp all the physics behind the SDI, the main physical parameters responsible for this interaction are also still largely unknown. Consequently, current models for the SDI introduce too many free parameters in order to describe, for example, how accretion rates and magnetic fields vary with time. Additionally, these models are typically for stars at around one solar mass, and the parameter space covered by them is insufficient for a full description of the whole mass-range we investigated here.

Finally, the predicted evolution of spin rates during the SDI will likely be different from a constant rotation if full SDI torques are included in the models (see Gallet et al. 2019, figs 4 and 5), but the qualitative results presented here should be robust, i.e., if external photoevaporation removes a disc from a star at an earlier age, the effects of the SDI will end earlier, and the star will be more subject to spin-up from its own contraction, as predicted by our model.

#### *4.1.2 Further mechanisms driving the dissipation of discs*

In the disc-dissipation model adopted in Section 2.1, WKC20 considered discs evolving due to the accretion process, along with the viscous spread of the material in the disc and FUV-induced external

photoevaporation of the material on the outer edge of the disc. Fig. 2 showed that the disc-dissipation time-scale variations with the local FUV-flux are mass dependent at all FUV fluxes considered. This is translated into a mass dependent spin evolution, and explains the success of our model on reproducing the structures observed in the period-mass distributions of young clusters.

Yet, the disc-dissipation model adopted does not include all the physical mechanisms known to take part on the dissipation process of real discs. Other external drivers of disc photoevaporation, such as the extreme-UV radiation (EUV, $h\nu \geq 13.5$ eV), can also contribute to the discs dissipation. However, we note that the mass-loss rates scale with the external radius of the disc to the power of $\frac{3}{2}$ for the EUV and roughly linearly for FUV (e.g. Johnstone et al. 1998), hence the EUV contribution is only relevant at the earlier disc evolution, and the FUV photons are expected to dominate over higher energy photons once the disc has been sufficiently truncated from the outer edge. As further explored by Winter et al. (2018, see their fig. 12 and section 4.1) a few exceptions exist, and EUV should dominate over the FUV in extreme cases, either very close to high-mass stars, where $F_{\rm FUV} > 10^4$ $G_0$ and the contribution of FUV to the disc dissipation reaches a plateau, or under very low $F_{\rm FUV}$ (see also Störzer & Hollenbach 1999). In the former case, the contribution of the EUV to the external photoevaporation would reduce even more the short $\tau_D$ for the $10^4$ $G_0$ case presented in Fig. 2. In the latter case, while the EUV contribution would dominate, this contribution is still too small and should not significantly affect the derived $\tau_D$s. None of these cases should change the conclusions derived here.

Dynamical encounters have also been posited as an alternative mechanism to induce premature dispersal of discs in dense environments (Vincke & Pfalzner 2016). However, random encounters are far less efficient at depleting discs than external photoevaporation (Winter et al. 2018; Concha-Ramírez et al. 2019a). Encounters instead occur early during the dynamical decay of high order multiple systems to set initial conditions, rather than dispersal time-scales (Bate 2018). Supernovae offer another potential avenue for externally induced disc destruction (Close & Pittard 2017); however, empirical evidence for such destruction remains inconclusive (Ansdell et al. 2020).

Internal dispersal by mechanisms other than accretion also operate on protoplanetary discs and these may dominate the evolution at the end of the disc lifetime in the absence of external depletion (e.g. Clarke, Gendrin & Sotomayor 2001). Internal EUV (Alexander, Clarke & Pringle 2006), X-ray (Owen et al. 2010), and FUV irradiation (Gorti & Hollenbach 2009; Gorti, Dullemond & Hollenbach 2009) may all play a role in late stage disc dispersal (see Alexander et al. 2014 for a review). In addition, some fraction of the disc mass must go into planets, the formation of which must therefore play a role in disc dispersal.

The unknown contribution of these internal dispersal mechanisms to the disc-dissipation time-scales may conflict with the assumption in our disc-dissipation model of a maximum $\tau_D$ of 10 Myr for discs around stars of all masses. In particular, a stellar mass dependence of internal processes could help to explain the contrary-sense mass dependence in the period-mass distribution of the Upper Sco region (Fig. 5 and Section 3.3), where 1 $M_\odot$ stars are on average slower rotators than 1.1–1.3 $M_\odot$ stars. Future studies considering the contribution of these internal processes may help improve spin-evolution models' capacity to fully reproduce the properties of observed data sets.

With the above considerations, the external FUV-driven winds should be interpreted as a process to systematically reduce the lifetimes of strongly irradiated discs in a statistical sense. Variations in disc evolution should introduce noise into this distribution, such that individual discs at single FUV flux may be depleted faster or slower by other influences. None the less, observations indicate that gradients in disc lifetimes with FUV flux are still present (e.g. Fang et al. 2012; Guarcello et al. 2016). The external irradiation of discs therefore remains a relevant factor in disc dispersal and therefore stellar rotation periods.

#### *4.1.3 Rigid-body rotation and the rotational evolution of MS stars*

In the Baraffe et al. (2015) evolutionary tracks, solar-type stars ($M_* \geq 0.3$ $M_\odot$) will eventually form a radiative core. Consequently, by assuming rigid-body rotation for the whole 0.1–1.3 $M_\odot$ range, we are treating these solar-type stars with their core and envelope rotating coupled to each other, with an instantaneous redistribution of angular momentum in the two regions. More robust treatments for the internal redistribution of angular momentum exist in the literature. For example, the widely used two-zone models (e.g. MacGregor & Brenner 1991; Allain 1998; Denissenkov 2010; Denissenkov et al. 2010; Spada et al. 2011; Gallet & Bouvier 2013, 2015; Lanzafame & Spada 2015; Spada & Lanzafame 2020) consider the internal structure of solar-type stars with a radiative core and a convective zone, which both rotate as solid-bodies at all ages, but can assume distinct spin rates. Inside this framework, the core and envelope decouple shortly after the formation of the radiative core and, as the star evolves through the PMS, angular momentum gets hidden in a faster-rotating core while the slower rotating convective envelope is kept under the break-up limit (see Gallet & Bouvier 2013, 2015). Two-zone models are typically parametrized by a core-envelope coupling time-scale, $\tau_{\rm ce}$, which indicates the rate of angular momentum exchange between the core and the envelope. Alternatively, a number of authors attempted to account for a full differential rotation in the radiative region (e.g. Pinsonneault, Kawaler & Demarque 1990; Denissenkov et al. 2010; Somers & Pinsonneault 2016; Eggenberger, Buldgen & Salmon 2019; Amard et al. 2019; Dumont et al. 2021; Gossage et al. 2021). However, we identified that every internal angular momentum transport description currently available in the literature include some initial condition or calibration constant derived while assuming that the environmental influence on rotation is negligible.

For example, most models include parameters, such as the $\tau_{\rm ce}$ in the two-zone models, derived by tuning or fitting spin evolution models to observed clusters. In this process, distributions of spin rates in clusters at different ages are assembled as an evolutionary sequence, which assumes that the environmental influence on rotation is negligible and that clusters with varied environments can be considered part of the same evolutionary sequence. Gallet & Bouvier (2013, 2015), for instance, had both $\tau_{\rm ce}$ and disc-locking duration as free parameters, which, along with the initial rotation and a calibration constant of the wind braking law, were simultaneously tuned to reproduce observations. Hence, any disc dissipation time-scales variation induced by the environment would go unnoticed behind the interplay between disc-dissipation time-scale and $\tau_{\rm ce}$ used as free parameters. Alternatively, Lanzafame & Spada (2015) derived a scaling relation between $\tau_{\rm ce}$ and stellar mass, using the Monte Carlo Markov chain method to fit spin evolution models to observations (see also Spada & Lanzafame 2020). However, their model assumed a fixed disc-locking duration of 5 Myr for all masses as an initial condition, which is inadequate to describe the rotation distributions of PMS clusters, as we have shown in Section 3.2. Finally, in order to avoid the uncertainties regarding the SDI phase, some authors start their spin-evolution model from the rotational distribution of h Per

(e.g. Somers & Pinsonneault 2016; Gossage et al. 2021). However, we have shown in Section 3.3 that h Per presents rotational properties compatible with a high-FUV environment, resulting in excess of fast rotating stars in h Per when compared to other clusters and it may not be an appropriate initial condition for MS clusters who had low or intermediate FUV environments during the PMS phase.

As the aim of this study was to probe the influence of the local-FUV environment on the spin evolution of stars, the model presented in Section 2 was designed while explicitly avoiding the inclusion of physical descriptions that are calibrated to reproduce distributions of spin rates in evolutionary sequences composed by clusters, such as the two-zone model for the internal structure of solar-type stars. By doing so, we were able to introduce the environmental influence on the SDI phase a priori and explore its long-term impact on the rotation history of stars at different masses while avoiding biasing our model with physical prescriptions calibrated while ignoring environmental effects.

Avoiding a core-envelope decoupling prescription comes at the expense of our models failing to reproduce some features visible in the period-mass distributions of MS clusters. One such feature is a dearth of stars observed at intermediate rotation periods between one and 6 d, forming a gap in the period-mass distributions of MS clusters, along with an enlarged $\Delta P$ between the fastest and slowest rotators at intermediate stellar masses. This gap is visible in the period-mass distributions of the Pleiades and Praesepe (Figs 1 and 5), and it suggests a more rapid spin-down just before convergence on the slow sequence (Barnes 2003). A more rapid spin-down may be caused, for example, by a modification to the external torque (e.g. Brown 2014; Gondoin 2017; Garraffo et al. 2018) or by a decoupling of the outer convection zone from the core (i.e. by relaxing the assumption of solid-body rotation; Gallet & Bouvier 2013, 2015).

Another important issue is that at 1 Gyr, our models have spun down more than the observed stars in NGC 6811. The observational evidence for this stalled spin-down has been largely debated in recent years (Agüeros et al. 2018; Douglas et al. 2019; Curtis et al. 2019), and a possible explanation for it is the interplay between core-envelope decoupling and the spin-down via magnetized winds. Such as, under the framework of the core-envelope theory, the resurfacing of angular momentum stored in the stellar core at later ages would compensate for the spin-down due to magnetized winds, temporarily stalling the stellar spin-down (Spada & Lanzafame 2020).

Finally, considering treatments for the internal redistribution of angular momentum that differ from a rigid body would offer an alternative workaround for the assumption of spin-up saturation at the break-up limit introduced in Section 2.2. By allowing for angular momentum to be stored in a faster rotating core, the surface can be prevented from reaching the break-up limit at the end of the spin-up phase, which would naturally avoid the convergence of high-FUV models, discussed in Section 3.1.5.

#### 4.1.4 Convective turnover time-scale

A final caveat in the model is our choice of convective turnover time-scale. By following MBB15, we adopted the prescriptions of Cranmer & Saar (2011), which provide $\tau_{cz}$ as a function of effective temperature for the temperature range 3300–7000 K. Yet, we adopted their prescription even for stars down to 0.1 $M_\odot$, which have lower effective temperatures. Cranmer & Saar (2011) provide comparisons between their estimations of $\tau_{cz}$ and other literature derivations (see Cranmer & Saar 2011, fig. 6). Their $\tau_{cz}$ ~70 Myr for a ~3000 K star is consistent with derivations by Reiners, Basri & Browning (2009) for M-dwarfs, but it is 2–3 times lower than the derivations by Barnes & Kim (2010). The impact of an underestimated $\tau_{cz}$ for the lowest mass stars can be discussed in the context of equation (3). An increase of 2–3 times in $\tau_{cz}$ in our models would reduce the saturation limit by the same factor and increase the spin-down torque of unsaturated stars. In our models for 0.1 $M_\odot$ with a slow initial rotation of 16 d, stars spend their first ~2 Myr in the unsaturated regime but become saturated as soon as they start to spin-up, only returning to the unsaturated regime after ~3 Gyr of spin evolution. At the earliest stages, the contribution of the wind-torque to the spin evolution of PMS stars is minimal. At the later stages, the 2–3 factor increase in $\tau_{cz}$ would cause the models to become unsaturated at later ages than the 4.5 Gyr final age of our model. None of these cases should inflict any significant changes to our results or conclusions.

#### 4.1.5 Distribution of low-mass stars in the neighbourhood of massive stars

In Section 3.4, we examined the influence of massive stars on the spin evolution of low-mass stars in their vicinity by looking at samples of equal-mass stars distributed in a Plummer sphere around single massive stars. In Fig. 7, we presented snapshots at 13 Myr of the spin evolution of low-mass stars distributed around massive stars with 80, 26, and 10 $M_\odot$. These examples should be regarded as an exercise of application of our FUV-irradiated spin evolution models to generic populations rather than as attempts to precisely reproduce the FUV environments of real clusters. The latter would require more complex assumptions on the cluster geometry, population, and their evolution, which are beyond the scope of this paper but will be the subject of a forthcoming paper. For the moment, we refer the reader to the growing literature exploring the FUV environments of clusters.

Fatuzzo & Adams (2008) have explored the dependence of the FUV-distributions in young embedded clusters on the size of the cluster (total number of members, $N$), the initial mass function (IMF) and the extinction. In the solar neighbourhood, clusters are small ($N \lesssim 10^3$), and their IMFs are typically incomplete towards higher masses, with their FUV-distributions mainly dominated by the highest mass in the cluster. In this context, our examples with 10 and 26$M_\odot$ are a reasonable approximation for the expected scenarios in nearby clusters. In young massive clusters ($N \geq 10^4$), larger populations of massive stars are present, and assumptions regarding the IMF are required to assess their FUV distributions. In this regard, Fatuzzo & Adams (2008) found that shallower IMFs result in clusters with larger populations of massive stars and larger outputs of FUV radiation. The existence of an 80$M_\odot$ star in a cluster population would thus accompany a number of other high-mass stars expected to also contribute to the cluster's FUV distribution. Hence, for massive clusters, the rotational scenario is expected to be more complex than presented in Section 3.4, with broader distributions of FUV-fluxes resulting in wider distributions of $\tau_D$ and spin rates.

The FUV-environments of real clusters has also been addressed by Winter et al. (2018), who estimated FUV-fluxes as a function of local-number density in well-studied young clusters (see also Winter et al. 2019). The example in Section 3.4 considers a distribution of sources with a central density of 100 sources per $pc^3$, which only covers a small fraction of the number density versus FUV-flux expected in real clusters (see Winter et al. 2018, fig. 3). In this context, future studies should explore the rotational evolution of low mass stars in the context of this wider variety of cluster environments.

We acknowledge the existence of other density distributions in the literature, such as the Elson-Fall-Freeman distribution (EFF

Elson; Fall & Freeman 1987), which are arguably a better fit for the distribution of stars in young clusters (e.g. Elson et al. 1987; Mackey & Gilmore 2003a, b). The EFF distribution has a similar formulation to the Plummer sphere (equation 5), but with an exponent of $-\frac{\gamma+1}{2}$ rather than $-\frac{5}{2}$. $\gamma$ describes how sharply the density of sources diminishes with $r$, and $\gamma \approx 1.3-4$ for young clusters (c.f., Winter et al. 2018, table 1). The EFF distribution is equivalent to a Plummer sphere when $\gamma = 4$, and the example in Section 3.4 thus runs on the upper limit for how centrally concentrated young clusters typically are. Lower values of $\gamma$ would result in shallower distributions of FUV and wider spreads in spin rates.

Young clusters are embedded in parental gas and dust for a time-scale of 1–3 Myr (Allen et al. 2007). The extinction caused by this material can reduce the FUV irradiation experienced by neighbouring stars (e.g. Fatuzzo & Adams 2008; Ali & Harries 2019; Winter et al. 2019, 2020a), shielding discs from external photoevaporation for time-scales of 1–2 Myr (e.g. Clarke 2007; Winter et al. 2019). Our results, therefore, represent an upper limit for the fingerprints of the FUV environments on rotation. Considering extinction should yield longer disc-dissipation time-scales for discs affected by external photoevaporation, thus changing both how early mass dependence becomes evident in the period-mass distributions and the relative difference in $\tau_D$ at different masses. Nevertheless, this mass dependence should be robust against the effects of extinction, as the differences in $\tau_D$ for extreme FUV regimes are larger than the time-scale for which young clusters are still embedded. We also note that the distribution of parental material in clusters tends to be clumpy (e.g. Lada & Lada 2003), with cluster members being unevenly affected by extinction, which could help to explain the spread of rotation rates observed in young clusters at a fixed mass.

As high-mass stars evolve faster than low-mass stars, the scenarios analysed in Section 3.4 are only valid if discs affected by external photoevaporation are dissipated before the end of the high-mass stars lifetime. This question has been statistically addressed by Winter et al. (2020a, see their appendix A), who found that given the IMF of high-mass star-forming regions, even when their most massive star reaches the end of their lifetime, the region likely host at least another star responsible for an equivalent contribution to the local FUV radiation field, but with longer lifetime. In the case of the 80 $M_\odot$ star, while this star would have a lifetime of about 3.5 Myr, Fig. 2 has shown that under high FUV levels ($\gtrsim$5000 $G_0$), discs around low-mass stars over a wide mass range would be dissipated in shorter time-scales. Consequently, the results for stars within $\sim$1.5 pc from the massive stars (c.f. Fig. 6) would not be affected by considering the end of the massive star's life, while stars further away would have slightly longer $\tau_D$s.

A final issue to be considered is that as clusters undergo dynamical evolution, the relative positions between cluster members change with time, as does the FUV irradiance at the position of each individual star. The external photoevaporation of discs in the context of the dynamical evolution of clusters has been approached in the context of different stellar densities by Concha-Ramírez et al. (2019b, 2021). Fluctuations in the local FUV fluxes at the position of individual stars induced by this dynamical evolution have also been illustrated by Parker et al. (2021, see their fig 1.), who also analysed the evolution of disc fractions for star-forming regions with varied initial conditions. While the impact of the initial density of sources on the average local FUV field is pointed to as the main factor governing discs evolution, Parker et al. also demonstrated that small changes in the initial conditions of star-forming regions with identical initial densities could significantly change discs survival probabilities. Future studies should combine spin-evolution models with *N*-body simulations to address if the trends derived in this study are reliable within the context of dynamically evolving clusters.

### 4.2 Consequences of the environmental influence on rotation

#### *4.2.1 Environmentally dependent disc-locking duration*

An environmentally dependent disc-locking duration is the main novelty of our models. Nevertheless, the idea of a variable disc-locking duration is not new, and it has been explored by several studies presenting semi-empirical models for the spin evolution of low mass stars (Gallet & Bouvier 2015; Vasconcelos & Bouvier 2017). In particular, Gallet & Bouvier (2013, 2015) used the disc lifetime as a free parameter in their spin evolution model. Starting from the 25th, 50th, and 90th percentiles (fast, median, and slow rotators) of the rotational distribution of stars in the ONC ($\sim$1 Myr), they adjusted their disc-lifetime parameter to reproduce the properties of h Per rotational distribution at 13 Myr. They found that a variable disc-locking duration between 2 and 9 Myr was required to reproduce the ZAMS's broad rotational distributions. Their analysis focused on stars in the mass intervals 0.4–0.6 $M_\odot$, 0.7–0.9 $M_\odot$, and 0.9–1.1 $M_\odot$, and they found systematically longer disc-locking duration for the higher mass stars with median and slow rotation, but without significant difference with mass among the fast rotators. Notably, at a fixed mass range, Gallet & Bouvier found shorter disc-locking time-scales for faster initial spin rates. As a possible explanation, they discuss how a correlation between initial rotation rate and disc-locking duration could be an outcome from the SDI operating at the embedded phase, with more massive discs yielding shorter initial rotation rates and living longer. Similarly, a series of studies by Tu et al. (2015) and Johnstone et al. (2019, 2021) derived and applied disc-dissipation time-scales that scale with the initial spin rate of the stars, following the same trend of shorter disc lifetime for faster initial rotation.

In this paper, we give a step further by proposing that the variable disc-locking durations found by previous studies can be explained by the influence of the local FUV-field on the disc dissipation process. As discussed in Section 3.4, the presence of massive stars increases the FUV radiation field in their surroundings and introduces a distribution of local FUV-fluxes among neighbouring stars, shaped by the massive star luminosity and the relative positions between this massive star and its neighbours. In Figs 6 and 7, we have shown that as a consequence of these variations in the local FUV fluxes, the period-mass distributions of low-mass stars in their neighbourhood gets skewed towards fast rotation, with the slow rotation envelope of the distributions dominated by stars under lower FUV fluxes, which at fixed mass had longer disc-locking duration, and the fast rotation envelope dominated by stars under higher FUV fluxes, which had shorter disc-locking duration. This result provides an alternative explanation to the correlations between disc-locking duration and initial rotation rate found by previous studies.

All previous spin evolution models mentioned in this section include a two-zone description for the internal structure of solar-type stars, as described in Section 4.1.3, with the core-envelope coupling time-scale as a free parameter adjusted to fit the observed distributions of open clusters. Therefore, the shorter disc-locking duration of fast-rotating stars obtained by these authors comes entangled with core-envelope coupling time-scales that are shorter towards the faster rotators and longer towards lower mass stars. We suggest that future studies should review these core-envelope coupling time-scales to include the influence of the environment on the disc-dissipation time-scales and to understand how this can

impact other free parameters in the spin evolution models. This is important not only for a correct understanding of the core-envelope coupling phenomenology while considering the impact of the environment on the rotational history of stars, but also for improving our capacity of reproducing the rotational properties of MS clusters,

#### *4.2.2 Implications for lithium depletion*

A number of previous of studies have suggested that the amount of lithium depletion measured in solar-type stars is closely related to their rotational history (e.g. Takeda et al. 2007; Bouvier 2008). In observations revealing a large dispersion of lithium abundances among stars in PMS and ZAMS clusters, fast-rotating stars are observed to be systematically less depleted in lithium than slowly rotating stars (e.g. Butler et al. 1987; Balachandran, Lambert & Stauffer 1988; Soderblom et al. 1993; Jones et al. 1997; Jeffries, James & Thurston 1998; Bouvier et al. 2016; Messina et al. 2016; Bouvier et al. 2018). These results have prompted the investigation of internal processes capable of explaining the trends observed, such as rotational mixing, internal magnetic fields and turbulence (e.g. Pinsonneault et al. 1990; Denissenkov et al. 2010; Somers & Pinsonneault 2016; Eggenberger et al. 2019; Dumont et al. 2021). In particular, the fact that a lithium-rotation connection has been observed in clusters as young as NGC 2264 (Bouvier et al. 2016) suggests that a physical process already acting at such young ages must be behind the observed lithium-rotation connection.

The impact of the disc lifetime on the lithium depletion of solar-type stars has been previously addressed by Eggenberger et al. (2012), who demonstrated that longer disc-locking durations increase the amount of differential rotation generated in the radiative zone during the disc-locking phase, resulting in more efficient rotational mixing and augmented lithium depletion during the PMS phase. Following this line, the environmentally induced variations on the disc-dissipation time-scales explored in the present study offer a plausible explanation for the dispersion in lithium abundances observed in open clusters.

An extra example supporting this hypothesis is the case of the lithium abundances in M67, which is a dense open cluster with a 3.5 Gyr age (Gaia Collaboration et al. 2018). As discussed by Somers & Pinsonneault (2016), M67 has a scatter in lithium abundances 1.4–4 times larger than younger clusters, depending on the effective temperature, that could not be reproduced by their spin evolution model calibrated by observations of younger clusters. Somers & Pinsonneault tested the hypothesis that M67 was richer in fast rotators than h Per, demonstrating that this intrinsically different rotational distribution at the age of h Per could explain the broad range of lithium abundances observed at 3.5 Gyr in the M67. Indeed, a study by Hurley et al. (2005) used *N*-body simulations to model M67 from formation to its current age, finding that an initial cluster mass of $2 \times 10^4$ $M_\odot$ gave the best results. This suggests that the cluster had a rich massive star population during its early-PMS phase and was susceptible to large amounts of FUV-radiation, which inside the framework of our model results, could explain the distribution of spin rates skewed towards fast rotation at the age of h Per suggested by Somers & Pinsonneault (2016).

We suggest that future observational studies should explore the distribution of lithium abundances in solar-type stars in the vicinity of massive stars, which could help to establish a link between FUV irradiance, lithium depletion and the rotational history of low mass stars. Such a link could mean that the fast rotation of highly FUV irradiated PMS stars may leave imprints in older MS stars even after they have converged to the slow rotating sequence (c.f. Pasquini, Randich & Pallavicini 1997).

#### *4.2.3 Open clusters at different ages may not be part of the same evolutionary sequence*

Extending from the examples of the effect of massive stars in their FUV environment, discussed in Section 3.4, clusters with varied populations of high-mass stars will have distinct FUV environments and, consequently, different rotational histories. This result corroborates the suggestion of Coker et al. (2016) of a cosmic variance in the distribution of spin rates in different clusters. For example, NGC 2264, which is the youngest cluster shown in Figs 1 and 5, has a total stellar mass of $\sim$530 $M_\odot$ (Sung & Bessell 2010; Dib 2014) and includes the S Monoceros binary system as its highest mass star, which is composed of a 26 $M_\odot$ and a $\sim$9 $M_\odot$ component. In contrast, h Per currently has a cluster mass of $\sim 1.6 \times 10^4$ $M_\odot$ (Portegies Zwart, McMillan & Gieles 2010). At 13 Myr, h Per has evolved beyond its first supernova explosion, having already lost its population with $M \gtrsim 10$ $M_\odot$. Nevertheless, the cluster's current mass function suggests the previous existence of a numerous and diverse massive-star population. A high-FUV environment induced by numerous massive stars during the early-PMS of h Per could explain the excess of fast-rotating stars in the cluster, which are likely related to the stars that were the most affected by the FUV field in the cluster's early ages.

The contrasting properties of NGC 2264 and h Per highlight a bias existent in the literature of spin evolution of low mass stars. While most young stars are found in clusters and associations, only a small fraction of these will survive the first $\sim$10 Myr (Lada & Lada 2003). Investigations of the physical processes leading to a cluster's disruption predict a dissolution time-scale that scales with the initial mass of the cluster (e.g. Lamers & Gieles 2006). During the first 10 Myr, clusters and associations are easy targets for photometric monitoring surveys, resulting in observations of period-mass distributions of clusters with a wide variety of environments, but with a bias towards regions with reduced stellar density, since crowded regions cause confusion in photometric surveys. At later ages, the ensemble of clusters observable gets biased towards a reduced variety of initial cluster properties and higher initial cluster mass, like the case of the M67 cluster.

From a theoretical perspective, in a follow-up study (Roquette, Matt & Winter, in preparation), we will use realistic initial mass functions and source distributions to simulate the FUV environment of clusters with varied massive star content and explore their rotational properties. From an observational perspective, we suggest that rotational surveys in young regions (3–10 Myr) rich in massive stars can help observationally establishing the role of high-FUV environments on the rotational history of low-mass stars. Furthermore, since the FUV-irradiance fingerprints on rotation are more robust for stars $M \lesssim 0.7$ M$\odot$, we highlight the importance of designing rotational surveys complete down to very low-mass stars. Finally, measuring the rotation rates for stars with $M_* \leq 0.4$ $M_\odot$ in h Per could significantly contribute to the field.

#### *4.2.4 Implications and applications for exoplanet populations*

Along with the stellar mass, rotation rate is empirically known to impact the X-ray emission and magnetic activity of low mass stars (Wright et al. 2011). Tu et al. (2015) demonstrated that initially

fast-rotating stars remain magnetically active for longer periods of time than slow rotating stars. The influence of rotation on the X-ray, EUV and Ly $\alpha$ emission can also impact the atmospheres of planets (e.g. Johnstone et al. 2015, 2021). For example, Johnstone (2020) recently showed that the longer magnetic activity of fast rotating stars can enhance the escape of water-vapour from the atmosphere of Earth-mass planets in the habitable zone. A correlation between high-FUV environments and faster stellar rotation could, therefore, have important impact on the atmosphere of Earth-mass exoplanets.

The premature destruction of discs by external photoevaporation may reduce the mass available for planet formation and even prevent planets from forming (Youdin & Goodman 2005; Johansen & Lambrechts 2017; Ormel, Liu & Schoonenberg 2017; Haworth et al. 2018a). More generally, if the rotational periods of stars are correlated with the time-scale of disc depletion by external mechanisms then this offers a unique window into the early stages of planet formation for mature planetary systems. In particular, a number of recent studies have claimed that stellar kinematics are correlated with exoplanet architectures (Winter et al. 2020b; Dai et al. 2021) that may relate to high-density stellar birth environments depending on the dispersal of kinematic substructure (e.g. Kamdar et al. 2019), efficiency of dynamical heating for open clusters (Tarricq et al. 2021), or initial clustering of open clusters in phase space (Coronado, Fürnkranz & Rix 2021). Enhanced hot Jupiter frequency, for example, may be the result of dynamical perturbation in clustered environments (Shara, Hurley & Mardling 2016; Brucalassi et al. 2016; Longmore et al. 2021; Rodet et al. 2021). However, the role of tidal inspiral and stellar ages on this finding remains debated (Adibekyan et al. 2021; Mustill, Lambrechts & Davies 2021; Winter & Alexander 2021).

Stellar rotation periods offer a window into environment versus age for the younger ($\lesssim$1 Gyr) stellar streams or open clusters that can be aged more accurately than single stars. Within such a population, slowly rotating stars may have retained a disc for longer during formation, which may then link environment with, for example, the mass distribution of the exoplanets (Kruijssen, Longmore & Chevance 2020). Hence, in light of our findings, we suggest that exoplanet surveys of open clusters (e.g. Quinn et al. 2012, 2014; Malavolta et al. 2016; Takarada et al. 2020) with well-quantified ages can be reconsidered in terms of the relative rotation periods of the surveyed stars. Such an exercise is particularly timely as *Gaia* uncovers more stellar streams (Kamdar, Conroy & Ting 2021) and the TESS mission uncovers the low mass planet population (Ricker et al. 2015).

#### *4.2.5 The mass dependence of rotation observed PMS clusters may not be a good proxy of age*

The observation of mass dependence in the period-mass distributions of young clusters along with the varying mass range in which this dependence is observed has led some authors to suggest that the slope of slow-rotation envelope of the period-mass distributions for stars $M_* \leq 0.5$ M$_\odot$ could be used as a proxy of age (Irwin et al. 2008; Henderson & Stassun 2012). In light of the results presented in Sections 3.3 and 3.4, we highlight that while this mass dependence does in fact evolve with age, the primary factor shaping this dependence is instead the FUV environment.

## 5 SUMMARY AND CONCLUSIONS

This study investigated the influence of the local FUV environment around massive stars on the spin evolution of low mass stars. We did so by updating the Matt et al. (2015) spin-evolution model to include a disc-locking phase in which the stars exchange angular momentum with their disc through the star-disc-interaction, keeping a constant rotation rate during this interaction. To constrain the duration of the disc-locking phase, we used the results of disc-dissipation models by Winter et al. (2020a), which give the evolution of viscous discs under the influence of external photoevaporation driven by the local FUV-radiation (Section 2.1). Due mainly to their shallower gravitational potential, external photoevaporation disperses discs around very low-mass stars more quickly than those around higher mass solar-type stars (Fig. 2).

We modelled the spin-evolution of stars evolving under five FUV fluxes of 10, 100, 1000, 5000, and 10 000G$_0$, considering discs with one-tenth of the stellar mass and viscous time-scales of 1, 2, and 5 Myr. We presented results in both rotation-age (Section 3.1 and Fig. 3) and rotation-mass (Section 3.2 and Fig. 4) parameter spaces. Our results demonstrate that the mass dependence introduced by the Winter et al. (2020a) disc-dissipation model translates into an intrinsically mass-dependent rotational evolution since the early-PMS phase (Fig. 4). The mass range affected by external photoevaporation increases with the local FUV flux. The variation of spin rate with mass is the most prominent at intermediate local FUV fluxes of 1000 G$_0$. For higher FUV fluxes of 5000 or 10 000G$_0$, stars of all masses lose their discs in less than 2–3 Myr of PMS evolution. Hence, at a given age, rotation rates are less dependent on mass at these high local FUV fluxes, but the period-mass distributions are faster-rotating overall when compared to lower local FUV fluxes. Future studies searching for observational evidence of the influence of the environment on rotation must acknowledge that to be observable in the period-mass distributions, stars that just got released from their discs need a few million years to spin-up enough to become distinguishable from the stars still locked to their discs in terms of their spin-up history.

The FUV-environment fingerprints are imprinted in the period-mass distributions until past the early-PMS phase and until MS stars converged to the slow-rotating sequence. At a fixed mass, stars influenced by their high-FUV environments started their spin-up phase earlier and, by having had more time to spin-up, reached the ZAMS as faster rotators. At later MS ages, these stars will also be the last ones of their mass range to converge to a slowly rotating sequence. Consequently, at a fixed age, the minimum mass at which the period-mass distribution converges to a slowly rotating sequence is larger for stars with higher FUV levels during their early-PMS phase. This feature is relevant to the field of exoplanets, as it brings up rotation rates as an observable link to the planet formation conditions for MS stars of order Gyr ages.

By comparing our models to the 5th and 95th rolling-percentiles of observed period-mass distributions in real clusters (Section 3.3 and Fig. 5), we verified that no single FUV model could simultaneously describe both populations of fast and slow rotators. Nevertheless, intermediate-FUV models can be claimed to explain the mass-dependent slow-rotation envelope of the period distributions of USco and NGC 2264. Moreover, the excess of fast-rotating stars at 13 Myr in h Per can be explained by a high FUV environment during the cluster's early-PMS evolution.

Finally, we used samples of low-mass stars distributed in a Plummer sphere around massive stars to explore the rotational evolution in their neighbourhood. We demonstrated how the presence of massive stars is responsible for skewing the period distributions towards fast rotation while introducing augmented mass-dependence in the period-mass distributions around higher mass massive stars. Observational studies exploring the distribution of rotation rates in massive star-forming regions can help to confirm our results,

especially if designed to include observations for very low-mass stars down to 0.1 $M_{\odot}$, which are the most affected by the FUV-environment.

Our results provide a cautionary tale to previously published rotational evolution models with physical parameters calibrated by assembling observations of spin rates for stars in different clusters as an evolutionary sequence. In particular, we suggest that models exploring the influence of rotation on the internal mixing of stars should further examine the PMS environment's potential to induce cosmic variance in cluster's properties, such as lithium abundances.

## ACKNOWLEDGEMENTS

We would like to thank Victor See, Mario Guarcello, Steven Rieder and Guilherme Maluf for useful discussions during the development of this work. We also thank the anonymous referee for their constructive suggestions that helped to improve this manuscript. JR, SS, SPM, and LA acknowledge funding from the European Research Council (ERC) under the European Union's Horizon 2020 research and innovation programme (grant agreement no. 682393 AWESoMeStars). AJW acknowledges funding from an Alexander von Humboldt Stiftung Postdoctoral Research Fellowship.

This research has made use of the SIMBAD database (Wenger et al. 2000), and of the VizieR catalogue access tool (Ochsenbein, Bauer & Marcout 2000), both operated at CDS, Strasbourg, France, and of the NASA's Astrophysics Data System Bibliographic Services.

*Software:* `ASTROPY` (Astropy Collaboration et al. 2013, 2018), `MATPLOTLIB` (Hunter 2007), `NUMPY` (Harris et al. 2020), `SCIPY` (Virtanen et al. 2020), `TOPCAT` (Taylor 2005)

## DATA AVAILABILITY

All the data and Python codes developed as part of this study are available as part of the package Far-ultraviolet Irradiated Rotational Evolution model for low mass stars (FIREstars) that can be accessible via https://github.com/juliaroquette/FIREstars. The package includes jupyter-notebooks with research notes on the project, computational tools for calculating spin-evolution models and isogyrochrones, along with the code used for producing each plot in the paper.

## REFERENCES

Adams F. C., 2010, ARA&A, 48, 47
Adams F. C., Hollenbach D., Laughlin G., Gorti U., 2004, ApJ, 611, 360
Adibekyan V. et al., 2021, A&A, 649, A111
Affer L., Micela G., Favata F., Flaccomio E., Bouvier J., 2013, MNRAS, 430, 1433
Agüeros M. A. et al., 2018, ApJ, 862, 33
Aigrain S., Hodgkin S., Irwin J., Hebb L., Irwin M., Favata F., Moraux E., Pont F., 2007, MNRAS, 375, 29
Alcalá J. M. et al., 2014, A&A, 561, A2
Alexander R. D., Clarke C. J., Pringle J. E., 2006, MNRAS, 369, 216
Alexander R., Pascucci I., Andrews S., Armitage P., Cieza L., 2014, in Beuther H., Klessen R. S., Dullemond C. P., Henning T., eds, Protostars and Planets VI, Vol. 914. University of Arizona Press, Tucson, p. 475
Ali A. A., Harries T. J., 2019, MNRAS, 487, 4890
Allain S., 1998, A&A, 333, 629
Allen L. et al., 2007, in Reipurth B., Jewitt D., Keil K., eds, Protostars and Planets V, Vol. 951. University of Arizona Press, Tucson, p. 361
Amard L., Palacios A., Charbonnel C., Gallet F., Bouvier J., 2016, A&A, 587, A105
Amard L., Palacios A., Charbonnel C., Gallet F., Georgy C., Lagarde N., Siess L., 2019, A&A, 631, A77
Andrews S. M., Rosenfeld K. A., Kraus A. L., Wilner D. J., 2013, ApJ, 771, 129
Ansdell M. et al., 2020, AJ, 160, 248
Ansdell M., Williams J. P., Manara C. F., Miotello A., Facchini S., van der Marel N., Testi L., van Dishoeck E. F., 2017, AJ, 153, 240
Armitage P. J., 2000, A&A, 362, 968
Armitage P. J., Clarke C. J., 1996, MNRAS, 280, 458
Astropy Collaboration et al., 2013, A&A, 558, A33
Astropy Collaboration et al., 2018, AJ, 156, 123
Attridge J. M., Herbst W., 1992, ApJ, 398, L61
Audard M. et al., 2014, in Beuther H., Klessen R. S., Dullemond C. P., Henning T., eds, Protostars and Planets VI, Vol. 914. University of Arizona Press, Tucson, p. 387
Balachandran S., Lambert D. L., Stauffer J. R., 1988, ApJ, 333, 267
Bally J., Sutherland R. S., Devine D., Johnstone D., 1998, AJ, 116, 293
Balog Z., Rieke G. H., Su K. Y. L., Muzerolle J., Young E. T., 2006, ApJ, 650, L83
Balog Z., Muzerolle J., Rieke G. H., Su K. Y. L., Young E. T., Megeath S. T., 2007, ApJ, 660, 1532
Baraffe I., Homeier D., Allard F., Chabrier G., 2015, A&A, 577, A42
Barnes S. A., 2003, ApJ, 586, 464
Barnes S. A., Kim Y.-C., 2010, ApJ, 721, 675
Barnes S. A., Spada F., Weingrill J., 2016, Astron. Nachr., 337, 810
Bate M. R., 2018, MNRAS, 475, 5618
Bertelli G., Bressan A., Chiosi C., Fagotto F., Nasi E., 1994, A&AS, 106, 275
Bodenheimer P., 1995, ARA&A, 33, 199
Bouvier J. et al., 2016, A&A, 590, A78
Bouvier J. et al., 2018, A&A, 613, A63
Bouvier J., 2008, A&A, 489, L53
Bouvier J., Cébron D., 2015, MNRAS, 453, 3720
Bouvier J., Forestini M., Allain S., 1997, A&A, 326, 1023
Bouvier J., Matt S. P., Mohanty S., Scholz A., Stassun K. G., Zanni C., 2014, in Beuther H., Klessen R. S., Dullemond C. P., Henning T., eds, Protostars and Planets VI, Vol. 914. University of Arizona Press, Tucson, p. 433
Brandt T. D., Huang C. X., 2015, ApJ, 807, 58
Breimann A. A., Matt S. P., Naylor T., 2021, AJ, 913, 75
Brown T. M., 2014, ApJ, 789, 101
Brucalassi A. et al., 2016, A&A, 592, L1
Butler R. P., Cohen R. D., Duncan D. K., Marcy G. W., 1987, ApJ, 319, L19
Cantat-Gaudin T. et al., 2018, A&A, 618, A93
Chevance M., Kruijssen J. M. D., Longmore S. N., 2021, ApJ, 910, L19
Cieza L., Baliber N., 2007, ApJ, 671, 605
Clarke C. J., 2007, MNRAS, 376, 1350
Clarke C. J., Gendrin A., Sotomayor M., 2001, MNRAS, 328, 485
Close J. L., Pittard J. M., 2017, MNRAS, 469, 1117
Cody A. M., Hillenbrand L. A., 2010, ApJS, 191, 389
Coker C. T., Pinsonneault M., Terndrup D. M., 2016, ApJ, 833, 122
Collier Cameron A., Campbell C. G., 1993, A&A, 274, 309
Concha-Ramírez F., Vaher E., Portegies Zwart S., 2019a, MNRAS, 482, 732
Concha-Ramírez F., Wilhelm M. J. C., Portegies Zwart S., Haworth T. J., 2019b, MNRAS, 490, 5678
Concha-Ramírez F., Wilhelm M. J. C., Portegies Zwart S., van Terwisga S. E., Hacar A., 2021, MNRAS, 501, 1782
Coronado J., Fürnkranz V., Rix H.-W., 2021, preprint (arXiv:2107.00036)
Covey K. R., Greene T. P., Doppmann G. W., Lada C. J., 2005, AJ, 129, 2765
Cranmer S. R., Saar S. H., 2011, ApJ, 741, 54
Currie T. et al., 2010, ApJS, 186, 191
Curtis J. L., Agüeros M. A., Douglas S. T., Meibom S., 2019, ApJ, 879, 49
Dai Y.-Z., Liu H.-G., An D.-S., Zhou J.-L., 2021, AJ, 162, 46
Damiani F., Prisinzano L., Pillitteri I., Micela G., Sciortino S., 2019, A&A, 623, A112
Delorme P., Collier Cameron A., Hebb L., Rostron J., Lister T. A., Norton A. J., Pollacco D., West R. G., 2011, MNRAS, 413, 2218
Denissenkov P. A., 2010, ApJ, 719, 28
Denissenkov P. A., Pinsonneault M., Terndrup D. M., Newsham G., 2010, ApJ, 716, 1269
Dib S., 2014, MNRAS, 444, 1957

Douglas S. T., Curtis J. L., Agüeros M. A., Cargile P. A., Brewer J. M., Meibom S., Jansen T., 2019, ApJ, 879, 100
Dumont T., Palacios A., Charbonnel C., Richard O., Amard L., Augustson K., Mathis S., 2021, A&A, 646, A48
Edwards S. et al., 1993, AJ, 106, 372
Eggenberger P., Haemmerlé L., Meynet G., Maeder A., 2012, A&A, 539, A70
Eggenberger P., Buldgen G., Salmon S. J. A. J., 2019, A&A, 626, L1
Eisner J. A. et al., 2018, ApJ, 860, 77
Elson R. A. W., Fall S. M., Freeman K. C., 1987, ApJ, 323, 54
Evans Neal J. I. et al., 2009, ApJS, 181, 321
Facchini S., Clarke C. J., Bisbas T. G., 2016, MNRAS, 457, 3593
Fang M. et al., 2012, A&A, 539, A119
Fang M., van Boekel R., Wang W., Carmona A., Sicilia-Aguilar A., Henning T., 2009, A&A, 504, 461
Fatuzzo M., Adams F. C., 2008, ApJ, 675, 1361
Feiden G. A., 2016, A&A, 593, A99
Flewelling H. A. et al., 2020, ApJS, 251, 7
Gaia Collaboration et al., 2018, A&A, 616, A10
Gallet F., Bouvier J., 2013, A&A, 556, A36
Gallet F., Bouvier J., 2015, A&A, 577, A98
Gallet F., Zanni C., Amard L., 2019, A&A, 632, A6
Garraffo C. et al., 2018, ApJ, 862, 90
Ghosh P., Lamb F. K., 1979, ApJ, 234, 296
Gondoin P., 2017, A&A, 599, A122
Gorti U., Hollenbach D., 2009, ApJ, 690, 1539
Gorti U., Dullemond C. P., Hollenbach D., 2009, ApJ, 705, 1237
Gossage S., Dotter A., Garraffo C., Drake J. J., Douglas S., Conroy C., 2021, ApJ, 912, 65
Guarcello M. G. et al., 2016, preprint (arXiv:1605.01773)
Guarcello M. G., Micela G., Peres G., Prisinzano L., Sciortino S., 2010, A&A, 521, A61
Guarcello M. G., Drake J. J., Wright N. J., García-Alvarez D., Kraemer K. E., 2014, ApJ, 793, 56
Habing H. J., 1968, Bull. Astron. Inst. Netherlands, 19, 421
Harris C. R. et al., 2020, Nature, 585, 357
Hartmann L., Herczeg G., Calvet N., 2016, ARA&A, 54, 135
Haworth T. J., Clarke C. J., 2019, MNRAS, 485, 3895
Haworth T. J., Facchini S., Clarke C. J., Mohanty S., 2018a, MNRAS, 475, 5460
Haworth T. J., Clarke C. J., Rahman W., Winter A. J., Facchini S., 2018b, MNRAS, 481, 452
Haworth T. J., Kim J. S., Winter A. J., Hines D. C., Clarke C. J., Sellek A. D., Ballabio G., Stapelfeldt K. R., 2021, MNRAS, 501, 3502
Henderson C. B., Stassun K. G., 2012, ApJ, 747, 51
Herbig G. H., 1977, ApJ, 217, 693
Hollenbach D. J., Tielens A. G. G. M., 1997, ARA&A, 35, 179
Hunter J. D., 2007, Comput. Sci. Eng., 9, 90
Hurley J. R., Pols O. R., Aarseth S. J., Tout C. A., 2005, MNRAS, 363, 293
Ireland L. G., Zanni C., Matt S. P., Pantolmos G., 2021, ApJ, 906, 4
Irwin J., Bouvier J., 2009, in Mamajek E. E., Soderblom D. R., Wyse R. F. G., eds, The Ages of Stars, Proceedings of the International Astronomical Union, IAU Symposium, Volume 258, p. 363
Irwin J., Hodgkin S., Aigrain S., Bouvier J., Hebb L., Irwin M., Moraux E., 2008, MNRAS, 384, 675
Jeffries R. D., James D. J., Thurston M. R., 1998, MNRAS, 300, 550
Johansen A., Lambrechts M., 2017, Ann. Rev. Earth Planet. Sci., 45, 359
Johnstone C. P. et al., 2015, ApJ, 815, L12
Johnstone C. P., 2020, ApJ, 890, 79
Johnstone D., Hollenbach D., Bally J., 1998, ApJ, 499, 758
Johnstone C. P., Pilat-Lohinger E., Lüftinger T., Güdel M., Stökl A., 2019, A&A, 626, A22
Johnstone C. P., Bartel M., Güdel M., 2021, A&A, 649, A96
Jones B. F., Fischer D., Shetrone M., Soderblom D. R., 1997, AJ, 114, 352
Kamdar H., Conroy C., Ting Y.-S., Bonaca A., Smith M. C., Brown A. G. A., 2019, ApJ, 884, L42
Kamdar H., Conroy C., Ting Y.-S., 2021, preprint (arXiv:2106.02050)
Kearns K. E., Eaton N. L., Herbst W., Mazzurco C. J., 1997, AJ, 114, 1098
Kim J. S., Clarke C. J., Fang M., Facchini S., 2016, ApJ, 826, L15
Koenigl A., 1991, ApJ, 370, L39
Kruijssen J. M. D., Longmore S. N., Chevance M., 2020, ApJ, 905, L18
Lada C. J., Lada E. A., 2003, ARA&A, 41, 57
Lamers H. J. G. L. M., Gieles M., 2006, A&A, 455, L17
Lamm M. H., Bailer-Jones C. A. L., Mundt R., Herbst W., Scholz A., 2004, A&A, 417, 557
Lamm M. H., Mundt R., Bailer-Jones C. A. L., Herbst W., 2005, A&A, 430, 1005
Landin N. R., Mendes L. T. S., Vaz L. P. R., Alencar S. H. P., 2016, A&A, 586, A96
Lanzafame A. C., Spada F., 2015, A&A, 584, A30
Longmore S. N., Chevance M., Kruijssen J. M. D., 2021, ApJ, 911, L16
Lynden-Bell D., Pringle J. E., 1974, MNRAS, 168, 603
MacGregor K. B., Brenner M., 1991, ApJ, 376, 204
Mackey A. D., Gilmore G. F., 2003a, MNRAS, 338, 85
Mackey A. D., Gilmore G. F., 2003b, MNRAS, 338, 120
Maeder A., 2009, Physics, Formation and Evolution of Rotating Stars, Springer Berlin Heidelberg
Makidon R. B., Rebull L. M., Strom S. E., Adams M. T., Patten B. M., 2004, AJ, 127, 2228
Malavolta L. et al., 2016, A&A, 588, A118
Manara C. F. et al., 2017, A&A, 604, A127
Mann R. K. et al., 2014, ApJ, 784, 82
Mathieu R. D., 2004, in Maeder A., Eenens P., eds, Stellar Rotation, Proceedings of IAU Symposium No. 215, held 11-15 November, 2002 in Cancun, Yucatan. Astronomical Society of the Pacific, San Francisco, p. 113
Matt S., Pudritz R. E., 2005, ApJ, 632, L135
Matt S. P., Pinzón G., de la Reza R., Greene T. P., 2010, ApJ, 714, 989
Matt S. P., Pinzón G., Greene T. P., Pudritz R. E., 2012, ApJ, 745, 101
Matt S. P., Brun A. S., Baraffe I., Bouvier J., Chabrier G., 2015, ApJ, 799, L23 (MBB15)
Mayne N. J., Naylor T., 2008, MNRAS, 386, 261
Messina S. et al., 2016, A&A, 596, A29
Moore K., Scholz A., Jayawardhana R., 2019, ApJ, 872, 159
Moraux E. et al., 2013, A&A, 560, A13
Mustill A. J., Lambrechts M., Davies M. B., 2021, preprint (arXiv:2103.15823)
Najita J. R., Kenyon S. J., 2014, MNRAS, 445, 3315
Natta A., Grinin V., Mannings V., 2000, in Mannings V., Boss A. P., Russell S. S., eds, Protostars and Planets IV. University of Arizona Press, Tucson, p. 559
Natta A., Testi L., Randich S., 2006, A&A, 452, 245
Nicholson R. B., Parker R. J., Church R. P., Davies M. B., Fearon N. M., Walton S. R. J., 2019, MNRAS, 485, 4893
Ochsenbein F., Bauer P., Marcout J., 2000, A&AS, 143, 23
Ormel C. W., Liu B., Schoonenberg D., 2017, A&A, 604, A1
Owen J. E., Ercolano B., Clarke C. J., Alexander R. D., 2010, MNRAS, 401, 1415
Parker R. J., Nicholson R. B., Alcock H. L., 2021, MNRAS, 502, 2665
Parravano A., Hollenbach D. J., McKee C. F., 2003, ApJ, 584, 797
Pascucci I. et al., 2016, ApJ, 831, 125
Pasquini L., Randich S., Pallavicini R., 1997, A&A, 325, 535
Pinsonneault M. H., Kawaler S. D., Demarque P., 1990, ApJS, 74, 501
Plummer H. C., 1911, MNRAS, 71, 460
Portegies Zwart S. F., McMillan S. L. W., Gieles M., 2010, ARA&A, 48, 431
Preibisch T., Brown A. G. A., Bridges T., Guenther E., Zinnecker H., 2002, AJ, 124, 404
Quinn S. N. et al., 2012, ApJ, 756, L33
Quinn S. N. et al., 2014, ApJ, 787, 27
Rebull L. M. et al., 2002, AJ, 123, 1528
Rebull L. M. et al., 2016, AJ, 152, 113
Rebull L. M., Wolff S. C., Strom S. E., 2004, AJ, 127, 1029
Rebull L. M., Stauffer J. R., Megeath S. T., Hora J. L., Hartmann L., 2006, ApJ, 646, 297
Rebull L. M., Stauffer J. R., Hillenbrand L. A., Cody A. M., Bouvier J., Soderblom D. R., Pinsonneault M., Hebb L., 2017, ApJ, 839, 92

Rebull L. M., Stauffer J. R., Cody A. M., Hillenbrand L. A., David T. J., Pinsonneault M., 2018, AJ, 155, 196
Rebull L. M., Stauffer J. R., Cody A. M., Hillenbrand L. A., Bouvier J., Roggero N., David T. J., 2020, AJ, 159, 273
Reiners A., Basri G., Browning M., 2009, ApJ, 692, 538
Ricker G. R. et al., 2015, J. Astron. Telesc. Instr. Syst., 1, 014003
Rigliaco E., Natta A., Randich S., Sacco G., 2009, A&A, 495, L13
Rigliaco E., Natta A., Randich S., Testi L., Biazzo K., 2011, A&A, 525, A47
Rodet L., Su Y., Lai D., 2021, ApJ, 913, 104
Rodríguez-Ledesma M. V., Mundt R., Eislöffel J., 2009, A&A, 502, 883
Rodríguez-Ledesma M. V., Mundt R., Eislöffel J., 2010, A&A, 515, A13
Roquette J., Bouvier J., Alencar S. H. P., Vaz L. P. R., Guarcello M. G., 2017, A&A, 603, A106
Sandquist E. L. et al., 2016, ApJ, 831, 11
Scholz A., Eislöffel J., 2004, A&A, 419, 249
Scholz A., Kostov V., Jayawardhana R., Mužić K., 2015, ApJ, 809, L29
Sellek A. D., Booth R. A., Clarke C. J., 2020, MNRAS, 492, 1279
Shara M. M., Hurley J. R., Mardling R. A., 2016, ApJ, 816, 59
Shu F., Najita J., Ostriker E., Wilkin F., Ruden S., Lizano S., 1994, ApJ, 429, 781
Skrutskie M. F. et al., 2006, AJ, 131, 1163
Skumanich A., 1972, ApJ, 171, 565
Smith N., Bally J., Morse J. A., 2003, ApJ, 587, L105
Soderblom D. R., Jones B. F., Balachandran S., Stauffer J. R., Duncan D. K., Fedele S. B., Hudon J. D., 1993, AJ, 106, 1059
Somers G., Pinsonneault M. H., 2016, ApJ, 829, 32
Sousa A. P. et al., 2016, A&A, 586, A47
Spada F., Lanzafame A. C., 2020, A&A, 636, A76
Spada F., Lanzafame A. C., Lanza A. F., Messina S., Collier Cameron A., 2011, MNRAS, 416, 447
Störzer H., Hollenbach D., 1999, ApJ, 515, 669
Sung H., Bessell M. S., 2010, AJ, 140, 2070
Sung H., Stauffer J. R., Bessell M. S., 2009, AJ, 138, 1116
Takarada T., Sato B., Omiya M., Hori Y., Fujii M. S., 2020, PASJ, 72, 104
Takeda Y., Kawanomoto S., Honda S., Ando H., Sakurai T., 2007, A&A, 468, 663
Tarricq Y. et al., 2021, A&A, 647, A19
Taylor M. B., 2005, in Shopbell P., Britton M., Ebert R., eds, ASP Conf. Ser. Vol. 347, Astronomical Data Analysis Software and Systems XIV. Astron. Soc. Pac., San Francisco, p. 29
Tinker J., Pinsonneault M., Terndrup D., 2002, ApJ, 564, 877
Tu L., Johnstone C. P., Güdel M., Lammer H., 2015, A&A, 577, L3
Vasconcelos M. J., Bouvier J., 2015, A&A, 578, A89
Vasconcelos M. J., Bouvier J., 2017, A&A, 600, A116
Venuti L. et al., 2014, A&A, 570, A82
Venuti L. et al., 2017, A&A, 599, A23
Vincke K., Pfalzner S., 2016, ApJ, 828, 48
Virtanen P. et al., 2020, Nature Methods, 17, 261
Wenger M. et al., 2000, A&AS, 143, 9
White R. J., Hillenbrand L. A., 2004, ApJ, 616, 998
Williams J. P., Cieza L. A., 2011, ARA&A, 49, 67
Winter A. J., Alexander R., 2021, MNRAS, 505, 869
Winter A. J., Clarke C. J., Rosotti G., Ih J., Facchini S., Haworth T. J., 2018, MNRAS, 478, 2700
Winter A. J., Clarke C. J., Rosotti G. P., 2019, MNRAS, 485, 1489
Winter A. J., Kruijssen J. M. D., Chevance M., Keller B. W., Longmore S. N., 2020a, MNRAS, 491, 903 (WKC20)
Winter A. J., Kruijssen J. M. D., Longmore S. N., Chevance M., 2020b, Nature, 586, 528
Wright N. J., Drake J. J., Mamajek E. E., Henry G. W., 2011, ApJ, 743, 48
Wright N. J., Drake J. J., Drew J. E., Guarcello M. G., Gutermuth R. A., Hora J. L., Kraemer K. E., 2012, ApJ, 746, L21
Yi I., 1994, ApJ, 422, 289
Youdin A. N., Goodman J., 2005, ApJ, 620, 459
Zanni C., Ferreira J., 2009, A&A, 508, 1117
Zanni C., Ferreira J., 2013, A&A, 550, A99

## APPENDIX A: OBSERVATIONAL DATA

In this section, we summarize the observational data used to compose (Figs 1 and 5). The references for the rotational distributions used are presented along with the parameters for the clusters and associations adopted for estimating stellar masses.

### A1 NGC 2264

The NGC 2264 cluster is ∼3 Myr old (Sung, Stauffer & Bessell 2009) and it is located at a distance $723^{+56}_{-49}$ pc (*Gaia* DR2; Cantat-Gaudin et al. 2018). NGC 2264 members had spin rates measured by multiple surveys, including ground- and space-based observations (e.g. Kearns et al. 1997; Makidon et al. 2004; Lamm et al. 2005; Affer et al. 2013; Sousa et al. 2016; Venuti et al. 2017). We adopted primarily spin rates derived by Venuti et al. (2017) based on data from the CoRoT Mission. However, in order to populate the whole mass-range of interest, we complemented the Venuti et al. data set with spin rates measured by Lamm et al. (2005), using $I_c$ light curves observed with the Wide Field Imager on the MPG/ESO 2.2 m telescope. The two surveys altogether provide spin rates for 522 stars in the mass range 0.1–1.3 $M_\odot$, 58 per cent of these had individual extinctions estimated by Venuti et al. (2014). When individual extinctions were not available, we adopted the Rebull et al. (2002) estimation of $E(B-V) = 0.146$ mag for cluster members. We derived masses primarily by comparing photometric observations to the isochrones of Baraffe et al. (2015). Pan-STARRS1 (Flewelling et al. 2020) i-band data was available for ∼ 78.5 per cent of the sample and was the main photometric band used for deriving masses. For the remaining stars, 12.7 per cent used the Pan-STARRS1 *g*- or *r*-band, 6 per cent used 2MASS (Skrutskie et al. 2006) *J*-band for disc-bearing stars, or Ks-band for discless stars, and when neither Pan-STARRS1 or 2MASS data was available (2.6 per cent), we converted effective temperature estimations provided by Venuti et al. (2014) into masses.

### A2 Upper Sco

Spin rates for member of the Upper Sco association were obtained by Rebull et al. (2018) as part of the NASA K2 mission. Ages in the range 5–10 Myr have been proposed in the literature (e.g. Preibisch et al. 2002; Feiden 2016), but we followed Rebull et al. (2018) and adopted an age of ∼8 Myr for USco members. A *Gaia* DR2 distance of 143 pc was adopted (Damiani et al. 2019). Rebull et al. (2018) also estimated individual extinctions for USco members using the 2MASS JHKs colour–colour diagram. When individual extinctions were not available, we adopted instead the association's mean reddening, $E(B-V) = 0.245$ mag. Rebull et al. (2018) also verified the presence of a circumstellar disc in 21 per cent of Upper Sco members. For discless stars, we derived masses by comparing 2MASS Ks observations to the Baraffe et al. (2015)'s isochrones. For disc-bearing stars, in order to avoid the near-infrared excess in the longer wavelengths, we derived masses based on 2MASS J observations.

### A3 h Per

Spin rates for the open cluster h Per (NGC 869) were derived by Moraux et al. (2013) as part of the MONITOR project (Aigrain et al. 2007). We estimated masses for cluster members by comparing 2MASS Ks observation to the Baraffe et al. (2015)'s isochrones while adopting the cluster's mean reddening, $E(B-V) = 0.54$ mag (Currie et al. 2010; Moraux et al. 2013), for all stars. We adopted an age of

13 Myr (Mayne & Naylor 2008; Moraux et al. 2013) for the cluster and the *Gaia* DR2 distance, $2336^{+712}_{-443}$ pc (Cantat-Gaudin et al. 2018).

### A4 Pleiades

Spin rates for Pleaide's members were obtained by Rebull et al. (2016) as part of the NASA K2 mission. We derived masses by comparing 2MASS Ks observation for cluster members to the Baraffe et al. (2015)'s isochrones, while adopting *Gaia* DR2 derivations of age (110 Myr), distance (136 pc), and reddening ($E(B-V) = 0.045$ mag) (Gaia Collaboration et al. 2018).

### A5 Praesepe

Spin rates for Praesepe's members were obtained by Rebull et al. (2017) as part of the NASA K2 mission. The age of Praesepe has been a matter of discussion in the literature. Isochrone fitting ages in the range ∼570–780 Myr have been previously obtained (e.g. Delorme et al. 2011; Brandt & Huang 2015), and a gyrochronology age of 670 Myr has been estimated by Douglas et al. (2019). Here, we adopted the *Gaia* DR2 derivation of age for the cluster (710 Myr), which is somehow in the middle of other values found in the literature. We derived masses by comparing 2MASS Ks observation for cluster members to the Baraffe et al. (2015)'s isochrones, while adopting the aforementioned age along with the *Gaia* DR2 distance (186 pc), and reddening ($E(B-V) = 0.027$ mag) (Gaia Collaboration et al. 2018).

### A6 NGC 6811

Spin rates for the open cluster NGC 6811 were obtained by Curtis et al. (2019) with data observed during the primary *Kepler* mission. We derived masses by comparing *Gaia* DR2 G magnitudes for cluster members to the Baraffe et al. (2015)'s isochrones. We adopted an age of 1 Gyr (Sandquist et al. 2016), the *Gaia* DR2 distance $1113^{+139}_{-111}$ pc (Cantat-Gaudin et al. 2018), and the cluster's mean extinction of $A_V = 0.15$ mag (Curtis et al. 2019).

## APPENDIX B: TABULATIONS FOR THE DISC-EVOLUTION TIME-SCALE

Table B1 presents tabulated results for the disc-dissipation models by Winter et al. (2020a), which is plotted in Fig. 2. Disc-dissipation time-scales ($\tau_{\rm FUV}$) are presented for stars with 0.1, 0.3, 0.5, 0.8, 1, and 1.3 $M_\odot$ evolving under FUV fluxes of 10, 100, 1000, 5000, and 10 000 $G_0$ for discs with viscous time-scales ($\tau_{\rm vis}$) of 1, 2, and 5 Myr.

**Table B1.** Disc-dissipation time-scales as a function of local FUV-flux and viscous time-scale for different stellar masses.

| $F_{\rm FUV}$ ($G_0$) | $\tau_{\rm FUV}$ (Myr) | | |
|---|---|---|---|
| | $\tau_{\rm vis}$=1 Myr | $\tau_{\rm vis}$=2 Myr | $\tau_{\rm vis}$=5 Myr |
| | | 0.1 $M_\odot$ | |
| 10 | 2.001 | 3.832 | 9.050 |
| 100 | 0.815 | 1.502 | 3.404 |
| 1000 | 0.332 | 0.596 | 1.285 |
| 5000 | 0.130 | 0.181 | 0.254 |
| 10000 | 0.019 | 0.019 | 0.020 |
| | | 0.3 $M_\odot$ | |
| 10 | 10.000 | 10.000 | 10.000 |
| 100 | 10.000 | 10.000 | 10.000 |
| 1000 | 2.068 | 4.360 | 10.000 |
| 5000 | 0.522 | 0.722 | 1.186 |
| 10000 | 0.271 | 0.391 | 0.623 |
| | | 0.5 $M_\odot$ | |
| 10 | 10.000 | 10.000 | 10.000 |
| 100 | 10.000 | 10.000 | 10.000 |
| 1000 | 3.699 | 7.032 | 10.000 |
| 5000 | 0.902 | 1.408 | 2.375 |
| 10000 | 0.481 | 0.628 | 0.818 |
| | | 0.8 $M_\odot$ | |
| 10 | 10.000 | 10.000 | 10.000 |
| 100 | 10.000 | 10.000 | 10.000 |
| 1000 | 10.000 | 10.000 | 10.000 |
| 5000 | 1.476 | 2.577 | 5.281 |
| 10000 | 0.666 | 0.959 | 1.441 |
| | | 1 $M_\odot$ | |
| 10 | 10.000 | 10.000 | 10.000 |
| 100 | 10.000 | 10.000 | 10.000 |
| 1000 | 8.966 | 10.000 | 10.000 |
| 5000 | 1.648 | 2.653 | 5.035 |
| 10000 | 1.255 | 1.817 | 2.779 |
| | | 1.3 $M_\odot$ | |
| 10 | 10.000 | 10.000 | 10.000 |
| 100 | 10.000 | 10.000 | 10.000 |
| 1000 | 10.000 | 10.000 | 10.000 |
| 5000 | 2.149 | 3.567 | 5.959 |
| 10000 | 1.357 | 1.806 | 2.861 |

This paper has been typeset from a TEX/LATEX file prepared by the author.